

Grid-based versus big region approach for inverting CO emissions using Measurement of Pollution in the Troposphere (MOPITT) data

T. Stavrakou¹ and J.-F. Müller¹

Received 17 November 2005; revised 20 April 2006; accepted 2 May 2006; published 8 August 2006.

[1] The CO columns retrieved by the Measurement of Pollution in the Troposphere (MOPITT) satellite instrument between May 2000 and April 2001 are used together with the Intermediate Model for the Annual and Global Evolution of Species (IMAGES) global chemistry transport model and its adjoint to provide top-down estimates for anthropogenic, biomass burning, and biogenic CO emissions on the global scale, as well as for the biogenic volatile organic compounds (VOC) fluxes, whose oxidation constitutes a major indirect CO source. For this purpose, the big region and grid-based Bayesian inversion methods are presented and compared. In the former setup, the monthly emissions over large geographical regions are quantified. In the grid-based setup, the fluxes are optimized at the spatial resolution of the model and on a monthly basis. Source-specific spatiotemporal correlations among errors on the prior emissions are introduced in order to better constrain the inversion problem. Both inversion techniques bring the model columns much closer to the measurements at all latitudes, but the grid-based analysis achieves a higher reduction of the overall model/data bias. Further comparisons with observed mixing ratios at NOAA Climate Monitoring and Diagnostics Laboratory and Global Atmosphere Watch sites, as well as with airborne measurements are also presented. The inferred emission estimates are weakly dependent on the prior errors and correlations. Our best estimate for the global CO source amounts to 2900 Tg CO/yr in both inversion approaches, about 5% higher than the prior. The global anthropogenic emission estimate is 18% larger than the prior, with the biggest increase for east Asia and a substantial decrease in south Asia. The vegetation fire emission estimates decrease as well, from the prior 467 Tg CO/yr to 450 Tg CO/yr in the grid-based solution and 434 Tg CO/yr in the monthly big region setup, mainly due to a significant reduction of African savanna fire emissions. The biogenic CO/VOC flux estimates are found to be enhanced by about 15% on the global scale. The most significant error reductions concern the biogenic emissions in the tropics, the Asian anthropogenic emissions, and the vegetation fire source over Africa. Our inversion results are further compared with previously reported emission estimates.

Citation: Stavrakou, T., and J.-F. Müller (2006), Grid-based versus big region approach for inverting CO emissions using Measurement of Pollution in the Troposphere (MOPITT) data, *J. Geophys. Res.*, *111*, D15304, doi:10.1029/2005JD006896.

1. Introduction

[2] Although pollution regulation measures call for a reduction in the emissions of a number of important greenhouse and greenhouse-related gases, the quantification of their emissions on the global scale is far from being complete and reliable. This is mainly due to the large spatiotemporal variability of sources and sinks, and the lack of a dense monitoring network which imposes the calculation of the emissions by models instead of measuring them directly. Therefore large uncertainties in the “bottom-up” emission inventories are generated by the assumptions for extrapolation of local and noncontinuous flux measurements of trace

gas fluxes to global-scale emissions. The “top-down” or inverse modeling approach consists in adjusting the surface emissions used as input in a chemistry transport model (CTM), in such a way that the discrepancy between a set of atmospheric observations and the model predictions becomes minimal. This is achieved by defining a set of emission parameters to be optimized and then minimizing a function of these parameters, which quantifies the overall discrepancy between the model and the data. The underlying assumption of this approach is that the model/data biases are mainly due to errors in the emission inventories. In this study, the “top-down” approach together with the Intermediate Model for the Annual and Global Evolution of Species (IMAGES) CTM are used in order to derive improved emissions for carbon monoxide using CO retrievals provided by the Measurement of Pollution in the Troposphere (MOPITT) satellite instrument onboard the EOS Terra spacecraft.

¹Belgian Institute for Space Aeronomy, Brussels, Belgium.

[3] Carbon monoxide (CO) plays a central role in tropospheric chemistry due to its contribution to ozone formation in the presence of nitrogen oxides and to its impact on hydroxyl radical (OH) concentrations, thereby affecting the lifetime and burden of other species (e.g., methane). Direct CO emissions are due to vegetation fires and the incomplete combustion of fossil fuels and biofuels. The major atmospheric photochemical sources of CO are the oxidation of methane and other hydrocarbons (e.g., isoprene). Less important sources include emissions from vegetation and soils on the continents and oxidation of organic matter in the oceans.

[4] Several CO inversion studies have been conducted in the last years using ground-based and airborne CO measurements at the global or the continental scale [Bergamaschi *et al.*, 2000; Pétron *et al.*, 2002; Kasibhatla *et al.*, 2002; Palmer *et al.*, 2003; Müller and Stavrakou, 2005], as well as data retrieved from satellite instruments [Pétron *et al.*, 2004; Arellano *et al.*, 2004; Heald *et al.*, 2004; Allen *et al.*, 2004]. The common tool of the aforementioned studies is the estimation of annual or monthly fluxes in relatively large predefined regions (big region approach). In this context, the number of control parameters to be determined by the inversion is generally small compared to the number of the observations. Note that this does not guarantee that the parameters are well resolved by the inversion, since overdeterminacy and underdeterminacy can take place simultaneously (see Rodgers [2000] for more details). The aggregation of fluxes over a few large regions implies that the emission distributions over these regions are those of the a priori inventory, and errors between the emissions of different grid cells within one region are assumed to be perfectly correlated (correlation coefficient equal to 1). Consequently, the prescribed a priori flux pattern within a given region cannot be improved by the inversion. The resulting “aggregation error” [Kaminski *et al.*, 2001] on the inferred fluxes constitutes a major limitation of the big region approach. In order to overcome this limitation, a significant increase in the number of control parameters is required, suggesting to move from the coarse resolution of the big region setup to the much finer resolution of the chemistry transport model itself. This approach is termed as “grid-based” inversion.

[5] This inversion technique has been used for long-lived gases, either unreactive (CO₂, Rödenbeck *et al.* [2003]) or weakly reactive (CH₄, Houweling *et al.* [1999]), using ground-based measurements and the adjoint of the transport scheme. The four-dimensional variational assimilation has been applied recently to synthetic satellite measurements of methane [Meirink *et al.*, 2005]. The adjoint model technique [Giering and Kaminski, 1998; Giering, 2000] proves to be a powerful tool in order to perform grid-based inversions, since it provides the only efficient way to compute sensitivities with respect to the control variables, when their number becomes very large. These inversion studies have demonstrated the potential of the adjoint-based framework to improve the emission estimates, but they also emphasized the need for atmospheric data sets of high density to adequately constrain the large number of unknowns.

[6] In this study, the quantification of CO fluxes is attempted using the IMAGES global model, the CO column retrievals from the MOPITT instrument, and two different

inversion methods: (1) the big region approach, where the monthly CO anthropogenic, biomass burning and biogenic emissions over large continental areas are quantified, and (2) the grid-based approach, where we optimize fluxes from every 5° × 5° model grid cell, for each month and for each emission process. In the latter case, although abundant satellite data are available, the inverse problem is underdetermined. The number of effective observational constraints is indeed much smaller than the actual number of MOPITT observational elements used in the inversion. In fact, due to the large chemical CO lifetime, as well as to the strong horizontal mixing in the troposphere, these pieces of information are not independent of each other. A way to better constrain the fluxes is to decrease the effective number of unknowns by introducing additional constraints in the form of correlations among prior errors of the control parameters. Contrary to the case of nonreactive species, CO is nonlinearly related to surface emissions, and the adjoint modeling framework including transport and chemistry is the best way to account for the response of CO to the changes in species interacting with it (e.g., OH). The full adjoint of the IMAGES model has been presented by Müller and Stavrakou [2005]. It is used in this study in both the big region and grid-based approaches. It is worth noting that, using the adjoint scheme, the time needed to determine the model sensitivity does not depend on the number of control variables to be determined, and is approximately the same for the two cases.

[7] To our knowledge, this is the first study addressing the problem of grid-based inversion of emissions of a reactive species at the global scale. Grid-based inversions offer an appealing alternative approach to the problem of estimating the emissions, provided that wide coverage data sets of high-quality measurements are available. The feasibility of the grid-based scheme for CO is demonstrated in this work and a comparison between the two inversion techniques is performed. The comparison highlights the capabilities but also the shortcomings of the inversion techniques to provide improved flux estimates.

[8] The remainder of the paper is organized as follows. Section 2 is devoted to a brief description of the IMAGES model and the “bottom-up” emission inventories used. The inversion methodologies, the specification of the particular setups and the satellite observations used to constrain the inversion are thoroughly discussed in Section 3. In Section 4, the resulting CO flux estimates are presented and their main features are explored. A posteriori errors are estimated and comparison of the results to independent observations and to previous inverse modeling studies is also conducted. To ensure that the results have a satisfactory degree of robustness, several sensitivity tests are performed and investigated in Section 5. Section 6 focuses on the advantages gained from the grid-based inversion and discusses future developments.

2. Model Description

2.1. IMAGES Model

[9] IMAGES is a global three-dimensional chemical transport model of the troposphere that provides the global distribution of 59 chemical constituents between the Earth's surface and the pressure level of 50 hPa [Müller and

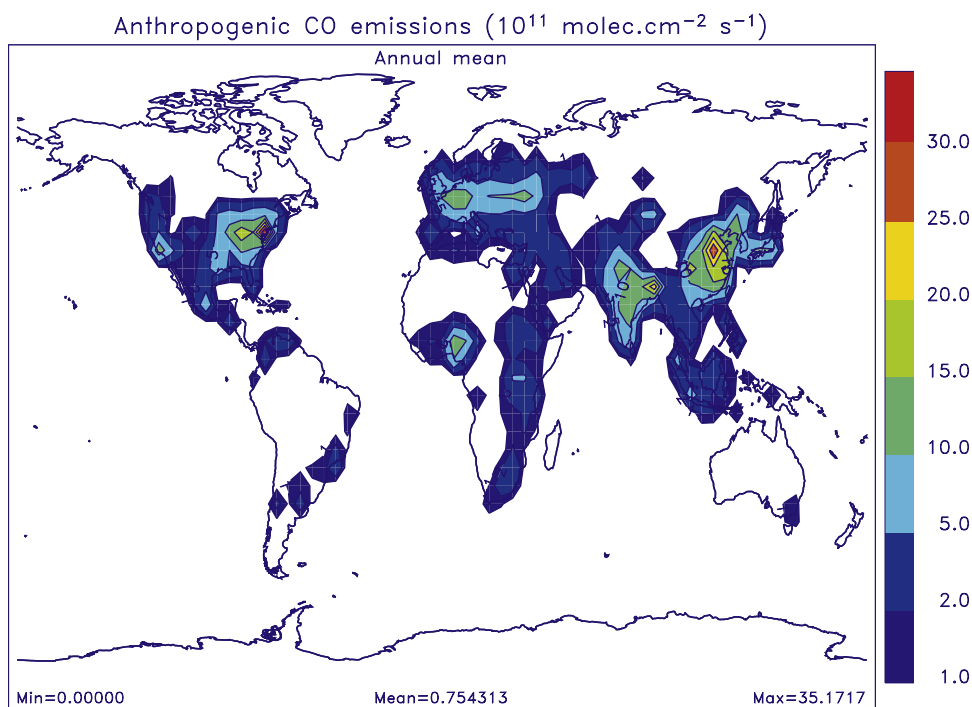


Figure 1. Annually averaged CO anthropogenic emissions (10^{11} molecules cm $^{-2}$ s $^{-1}$).

Brasseur, 1995]. The simulations are performed at a horizontal resolution of 5 degrees with 25 vertical layers and a time step equal to 1 day. Advection is represented using a semi-Lagrangian transport scheme [Smolarkiewicz and Rasch, 1991] driven by monthly mean European Centre for Medium-range Weather Forecasts (ECMWF) (ERA40) reanalyzed fields for the period from January 2000 to April 2001. The mixing of chemical compounds resulting from the temporal variability of the winds is introduced in the model via horizontal and vertical diffusion coefficients, estimated using the ECMWF wind variances. Turbulent mixing in the planetary boundary layer (PBL) is also parameterized as vertical diffusion. Convection is approached following the Costen *et al.* [1988] parameterization. The cloud updrafts are distributed according to the monthly averaged climatological (1983–2001) distributions of the cumulonimbus fractional cover provided by the International Satellite Cloud Climatology Project (ISCCP) (“D2” data set, see Rossow *et al.* [1996] and <http://isccp.giss.nasa.gov/products/isccpDsets.html>).

[10] The chemical transport model has been evaluated against ^{222}Rn and ^{85}Kr measurements in Müller and Brasseur [1995] and Friedl [1997], airborne measurements from Emmons *et al.* [2000] and Law *et al.* [2000], and other CTMs from Savage *et al.* [2003] and Kanakidou *et al.* [1998]. Recent updates and improvements of the model have been discussed by Müller and Stavrou [2005].

[11] Model runs include a spin-up time of 4 months, starting on 1 January 2000. The model results are evaluated against observations between 1 May 2000 and 30 April 2001.

2.2. A Priori Emissions

[12] Emissions for CO and VOCs from technological sources, biofuel use and agricultural waste burning are based on the 1997 EDGAR v3.3 inventory [Olivier and

Berdowski, 2001; Olivier *et al.*, 2001, 2003; Peters and Olivier, 2003; see also <http://www.mnp.nl/edgar/model/>]. This inventory has been compiled by using the corresponding inventory for 1995 and regional trend data for various sources (see Peters and Olivier [2003] for details on this approach). The seasonal variation of technological emissions is determined from the seasonal variation of fossil fuel consumption and production and from the temperature dependence of vehicle emissions following Müller [1992]. The annual mean of CO anthropogenic emissions is illustrated in Figure 1.

[13] The distribution of vegetation fires is taken from the Global Fire Emissions Database (GFED v1, Van der Werf *et al.* [2003], <http://www.ess.uci.edu/jranders/>) for the period between 1 January 2000 and 30 April 2001 (Figure 2). In this inventory, monthly carbon emissions from fires have been estimated at $1^\circ \times 1^\circ$ spatial resolution, by using satellite fire activity data converted into burned area, as an input to the CASA biogeochemical model. The CO emissions are computed using the biome-dependent emission factors provided by Andreae and Merlet [2001]. The estimated source for the May 2000 to April 2001 period is equal to 467 Tg CO/yr. To test the sensitivity of the inversion results against the a priori biomass burning inventory used, we conducted an additional inversion study using the POET inventory [Olivier *et al.*, 2003]. In this database, the distribution of burnt biomass follows the ATSR fire counts (<http://dup.esrin.esa.int/ionia/wfa/>). The emissions are scaled in such a way that the total CO $_2$ emissions averaged over the 1997–2001 period match the global annual emissions estimate provided by Hao and Liu [1994]. The CO $_2$ emissions are converted to CO emissions using the emission ratios provided by Andreae and Merlet [2001]. The source in the POET database is significantly

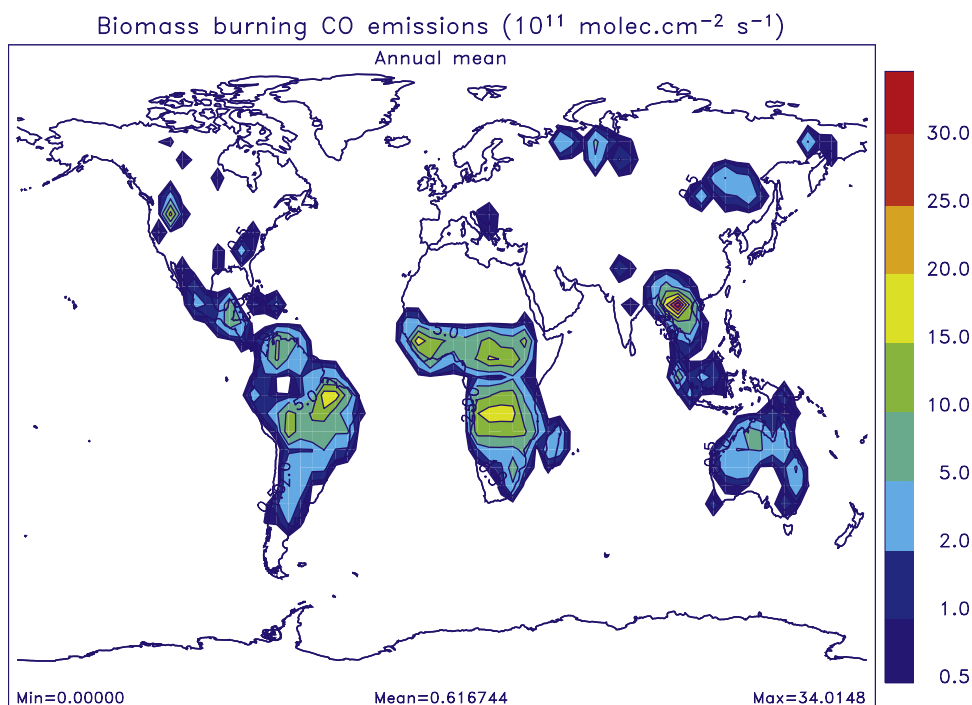


Figure 2. Annually averaged CO emissions from biomass burning over May 2000 to April 2001 (10^{11} molecules cm^{-2} s $^{-1}$).

lower than the GFED estimate and amounts to 272 Tg CO/yr for the period from May 2000 to April 2001.

[14] The anthropogenic source of methanol, derived by applying the emission ratios reported by *Jacob et al.* [2005] to the CO anthropogenic source, is estimated at 10 Tg/yr. The global biomass burning source of methanol is estimated to be 9.2 Tg/yr using the emission factors from *Andreae and Merlet* [2001] and the CO biomass burning inventory (GFED). Methanol from biogenic sources (plant growth and decay) is calculated by applying the emission factors used by *Jacob et al.* [2005] to the monthly mean net primary productivity (NPP) and heterotrophic respiration rates from the CASA model [*Randerson et al.*, 1997]. The resulting estimates amount to 130 and 22 Tg/yr for the plant growth and decay, respectively. We also used methanol deposition velocities over land (0.2 cm/s) and ocean (0.08 cm/s) from *Jacob et al.* [2005]. Dry deposition is calculated to represent about 40% of the total sink, in good agreement with *Jacob et al.* [2005]. The emissions represent a significant model-calculated photochemical source of CO amounting to ca. 90 Tg CO/yr.

[15] The biogenic emissions of isoprene and monoterpenes are taken from *Guenther et al.* [1995]. Their global estimates amount to 568 Tg/yr for isoprene and to 144 Tg/yr for monoterpenes. The yield of CO from isoprene and terpenes, calculated under high NO_x conditions, is about 50% and 44%, respectively. The NO_x emissions used in the model, as well as the dry deposition velocities of CO and NO_x are the optimized values derived from previous inversion study using the IMAGES model [*Müller and Stavrou, 2005*]. Direct biogenic CO emissions (mostly from soils) are taken from *Müller and Brasseur* [1995]. Ocean emissions of CO are distributed according to the ocean emission of CO derived by *Erickson* [1989].

[16] Surface boundary conditions for CH_4 are latitude and month dependent mixing ratios based on Climate Monitoring and Diagnostics Laboratory (CMDL) observations [*Granier et al.*, 2003].

[17] The a priori CO global budget used in this study is summarized in Table 1. In this study we optimize the anthropogenic and pyrogenic CO emissions, as well as the combined biogenic source of CO, isoprene, terpenes, and methanol. Note that the CO deposition velocity and oceanic emissions are not optimized.

3. Inversion Methodology and Setup

[18] The a priori emission distributions for a given species can be written as

$$G_0(x, t) = \sum_{j=1}^m \Phi_j(x, t), \quad (1)$$

where $\Phi_j(x, t)$ denote the a priori emission distributions used in the model, and x, t the space (latitude, longitude, altitude) and time (month) variables. The index $j = 1, \dots, m$ runs over the base functions. Each of these functions is multiplied by the exponential of a dimensionless control parameter f_j , so that the a posteriori flux estimate is expressed by the formula

$$G(x, t, f_j) = \sum_{j=1}^m \exp(f_j) \Phi_j(x, t). \quad (2)$$

We seek the set of parameter values that best satisfies two requirements: the optimized fluxes should be close enough to the prior “bottom-up” fluxes, and the resulting CO

Table 1. Results of Different Optimization Studies Using the GFED and POET Databases for Biomass Burning Emissions^a

Source Category	GFED				POET	
	A Priori	Grid Based	Big Region		A Priori	Grid Based
			Monthly	Annual		
Anthropogenic	571	664	685	675	571	688
Tropical fires	170	162	159	170	60	79
Savanna fires	268	257	249	214	190	296
Extratropical fires	29	31	26	28	23	29
Biogenic	160	199	200	186	160	195
Oceans	20	20	20	20	20	20
CH ₄ oxidation	796	761	772	770	802	755
NMVOCS oxidation	734	813	794	798	718	798
Total	2748	2907	2905	2861	2544	2860
Deposition	183	201	201	199	166	198
CO lifetime, days	49	51.2	50.7	51.4	48.8	51.7
CH ₄ lifetime, years	9.5	9.9	9.6	9.8	9.5	10
Isoprene, Tg/yr	568	657	620	639	568	665
Terpenes, Tg/yr	144	167	162	164	144	170
Methanol, Tg/yr	171	204	209	196	167	201

^aCO emission fluxes and deposition are expressed in Tg CO/yr.

atmospheric abundances should exhibit minimal deviation from the actual observed concentrations. The solution to this problem corresponds to the minimum of the cost function

$$\begin{aligned}
 J(\mathbf{f}) &= J_{obs}(\mathbf{f}) + J_B(\mathbf{f}) \\
 &= \frac{1}{2}(\mathbf{H}(\mathbf{f}) - \mathbf{y})^T \mathbf{E}^{-1}(\mathbf{H}(\mathbf{f}) - \mathbf{y}) \\
 &\quad + \frac{1}{2}(\mathbf{f} - \mathbf{f}_B)^T \mathbf{B}^{-1}(\mathbf{f} - \mathbf{f}_B),
 \end{aligned} \quad (3)$$

where \mathbf{E} , \mathbf{B} are the matrices of error estimates on the observations and the emission parameters, respectively, H is the forward model operator acting on the control variables, \mathbf{f}_B is the first guess value for the control parameters (taken equal to zero), and the superscript T means the transpose. Note that exponentiating the control variables f_j in equation (2) not only ensures the positiveness of the optimized fluxes but it also leads to a non-Gaussian distribution of the prior emission errors. Given that the forward model operator is not linear and the prior error estimates on the emission parameters are not normally distributed, the minimum of the cost function does not represent the maximum likelihood solution. Further, the resulting probability density function of the posterior fluxes is not Gaussian.

[19] The error covariance matrix \mathbf{E} , assumed diagonal, includes errors produced during the observation process as well as representativeness/model errors related to the operator H . The specification of the matrix \mathbf{B} requires knowledge about the a priori emission inventories, and reflects assumptions on the processes responsible for the estimated fluxes. As will be discussed later, this matrix will be either diagonal or nondiagonal, depending on the inversion setup.

[20] The adjoint of the model is used to calculate the gradient of J with respect to the parameter vector \mathbf{f} :

$$(\nabla J)_{\mathbf{f}} = (\mathbf{DH})_{\mathbf{f}}^T \mathbf{E}^{-1}(\mathbf{H}(\mathbf{f}) - \mathbf{y}) + \mathbf{B}^{-1}(\mathbf{f} - \mathbf{f}_B), \quad (4)$$

where $(\mathbf{DH})_{\mathbf{f}}$ is the derivative of H at \mathbf{f} viewed as a linear transformation (Jacobian matrix). The adjoint code is derived directly from the numerical code of the IMAGES model (see Müller and Stavrou [2005] for more details). The cost function and its gradient calculated by the forward

and adjoint models, respectively, are used as inputs in the minimization subroutine M1QN3 [Gilbert and Lemaréchal, 1989], in order to obtain an updated estimate for the parameter vector \mathbf{f} . The algorithm proceeds iteratively, until J reaches its minimum. The convergence criterion used in the optimization runs is a reduction by a factor of 1000 of the norm of the gradient of the cost function. The number of iterations needed to attain this criterion is dependent on the inversion scheme chosen. Note that although the optimization includes the spin-up period (January 2000 to April 2000), the model is compared to the data only for the period May 2000 to April 2001.

3.1. Observational Data Set

[21] CO columns derived from a subset of the L2V3 MOPITT profiles from May 2000 to April 2001 are used to constrain the inversion. The data are available from the NASA Langley Research Center Atmospheric Sciences Data Center (<http://www.eos.ucar.edu/mopitt/data/>). The retrieval algorithm has been discussed by Deeter *et al.* [2003] and validation of the retrievals has been performed with a varied set of airborne measurements [Emmons *et al.*, 2004]. Following the MOPITT data quality statement, our analysis takes into account only retrievals between 65°S to 65°N that have less than 50% contribution of the retrieval prior profile, and contain no less than seven vertical pressure levels. Because of the fact that the nighttime CO retrieval is closer to the a priori profile and shows less information content [Crawford *et al.*, 2004], only daytime measurements are considered in this study. Moreover, oceanic pixels are not taken into account due to the recognized artificial land/ocean bias introduced in the retrievals, attributed to changes in sensitivity of the measurement over different surfaces, as well as the highly biased MOPITT data at clean environments such as the South Pacific (Rarotonga, Hawaii) compared to aircraft measurements [Emmons *et al.*, 2004]. A sensitivity study, performed using MOPITT data over both land and ocean, shows that the results are not fundamentally affected by the omission of MOPITT data over the oceans.

[22] The individual CO columns and averaging kernels are binned onto the 5° × 5° horizontal grid of the IMAGES

model and monthly averaged. The model CO column is then calculated using the MOPITT averaging kernels. The use of these averaging kernels allows to take into account the higher sensitivity of the MOPITT retrievals to midtropospheric and upper tropospheric CO. As in the case of inversions using surface network observations, however, the model/data biases remain critically dependent on model errors influencing the vertical distributions of gases.

[23] A total of 5806 observations are used in the inversion analysis. The observation errors are considered as mutually uncorrelated. The errors represent a combination of the retrieval error reported in the MOPITT data set, and representation/model errors assumed at 50% of the observed CO column. Note, however, that in the case of a high-density observational data set, error correlations due to model errors (transport and chemistry) as well as to systematic biases in the MOPITT retrievals are not negligible [Heald *et al.*, 2004].

3.2. Grid-Based Approach

[24] In this inversion scheme, the fluxes are estimated at the resolution of the IMAGES model. The seasonality and geographical distribution of the emissions are varied. Here, $\Phi_j(x, t)$ of equation (1) are the fluxes emitted from every $5^\circ \times 5^\circ$ model grid cell, for each month, and for each emission process. A total number of 33,516 control variables are optimized in this setup, i.e., (1) monthly anthropogenic CO emissions (12,108 variables), (2) monthly biomass burning CO emissions (7260 variables), and (3) monthly biogenic CO and VOC (isoprene, monoterpenes, methanol) emissions (14,148 variables).

[25] Since the number of unknowns to be determined is higher than the number of independent MOPITT measurements used in this study, the inverse problem to be solved is underdetermined. We therefore introduce additional constraints in the form of correlations among prior errors on the control parameters. In this way, the effective number of control parameters is clearly reduced and the flux estimates are better constrained. A set of suitably defined spatiotemporal correlations among the a priori (background) errors on \mathbf{f} is used to construct the error covariance matrix \mathbf{B} of equation (3), as will be shown hereafter.

[26] Because of the large number of unknowns and the impact of correlations, the minimization procedure becomes extremely slow, more than 250 iterations are generally needed to obtain a reduction of the gradient of the cost function of only 100. To accelerate the convergence rate, we build a set of new uncorrelated control variables having unit variance (i.e., preconditioning), so that the value of the cost function expressed in the new variables remains invariable [Axelsson, 1994]. The preconditioning results in an impressive speed-up in the minimization convergence rate. Indeed, only 50 iterations are needed to satisfy the convergence criterion.

[27] The spatial and temporal correlations are considered here to be statistically independent: $\mathbf{B} = \mathbf{B}(r)\mathbf{B}(t)$, where $\mathbf{B}(r)$, $\mathbf{B}(t)$ are the spatial and temporal components, respectively. In addition, no cross correlations are assumed between the different emission categories.

3.2.1. Correlation Setup for Anthropogenic Emissions

[28] The spatial correlations are based on the assumption that the errors on the fluxes emitted from different grid cells

are highly correlated (0.85 or 0.7) when both grid cells belong to the same country, whereas the errors on the total emissions by different countries are assumed to be either weakly correlated (correlation of 0.3) when the countries belong to the same large region, or not correlated, in the other case. The regions are defined following the EDGAR3 subdivision of the world land: Canada, United States, Organisation for Economic Co-operation and Development Europe, Oceania, Japan, eastern Europe, former Soviet Union, Latin America, Africa, Middle East, south Asia, east Asia, SE Asia (<http://www.rivm.nl/edgar/documentation/>). It follows that the geographical distribution of the emissions within each country is assumed to be better known than their repartition at a larger scale. This choice reflects the assumption that the fine-scale distribution of the emissions is mainly determined by the distribution of the activity factors (like gasoline consumption, etc.), which can be expected to be relatively well known, whereas their larger-scale distribution reflects also differences in technological development, regulation measures and emission estimation procedures between different countries, especially when these countries belong to different world zones. We explain hereafter in detail the construction of the error covariance matrix.

[29] Let E_n be the total emission of country n , σ_{E_n} the standard error on this emission, and d_i^n the flux fraction emitted by the country n in the grid cell i , then the total flux emitted in the grid cell i is given by

$$\phi_i = \sum_n d_i^n E_n, \quad (5)$$

and the fraction of the flux emitted by the grid cell i and originates from country n is equal to

$$x_i^n = d_i^n E_n / \phi_i. \quad (6)$$

The diagonal elements of the error covariance matrix are defined as the square of the relative errors on the fluxes emitted by the grid cell i :

$$B_{ii}(r) = (\sigma_{\phi_i} / \phi_i)^2. \quad (7)$$

By straightforward calculation, we find that B_{ii} is equal to

$$B_{ii}(r) = \sum_n \sum_m A^{nm} x_i^n x_i^m (\sigma_{E_n} / E_n) (\sigma_{E_m} / E_m). \quad (8)$$

In equation (8), A^{nm} is equal to 1 when the countries n and m are identical and to 0.3 or 0 depending whether the countries n and m belong or not to the same big region. The relative error σ_{E_n} / E_n on the emissions of country n is taken equal to 0.35 for the group of industrialized countries (first 6 EDGAR3 regions) and to 0.6 for the remainder of the regions. As can be seen by equation (8), when more than one country is present in the same grid cell i , the terms corresponding to the contribution of each country are further compounded by extra terms representing cross correlations between errors on the emissions of different countries in the same region. Moreover, the relative error on the fluxes takes its maximal value when a grid cell

is entirely occupied by one country: in this case, $x_i^n = 1$ and $B_{ii} = (\sigma_{E_n}/E_n)^2$. The error decreases when the grid cell is occupied by more than one country, and it is further reduced in the case where no correlations are assumed.

[30] The off-diagonal terms B_{ij} correspond to the error correlation between fluxes emitted from different grid cells:

$$B_{ij}(r) = \sum_{n,m} C_{ij}^{nm} A^{nm} x_i^n x_j^m (\sigma_{E_n}/E_n)(\sigma_{E_m}/E_m). \quad (9)$$

The factor C_{ij}^{nm} is introduced in order to allow for some variations in the geographical distribution of emissions within a country. Its value is 0.85 when the countries n and m belong to the first 6 regions (industrialized countries), and 0.7 for the other countries where the distributions of the emissions are known with lesser certainty. It is equal to 1 when $i = j$, so that equation (9) reduces to equation (8).

[31] The diagonal terms of the temporal part of the error covariance matrix \mathbf{B} are taken equal to 1. For this emission category it is assumed that the temporal structure does not change from month to month. Therefore the off-diagonal terms $B_{ij}(t)$ of the matrix $\mathbf{B}(t)$, corresponding to the errors between the fluxes emitted in different months, are constant and equal to 0.9.

3.2.2. Correlation Setup for Biomass Burning Emissions

[32] The diagonal terms $B_{ii}(r)$ of the spatial error covariance matrix are the squares of the error on the flux parameter corresponding to the grid cell i . This error is taken to 0.7, to account for the high uncertainty related to the biomass burning source.

[33] The spatial correlations, implemented by the off-diagonal terms, are based on the geographical distance d_{ij} between grid cells i and j at which fluxes are to be estimated. This distance is calculated using the great circle arc on the surface of the Earth. We assume that correlations decay exponentially following the formula: $B_{ij}(r) = \exp(-d_{ij}/\ell)(\sigma_{\phi_i}/\phi_i)^2$. The decorrelation length ℓ is taken equal to 2000 km. Sensitivity studies will be conducted in order to test the impact of this choice in the inversion results. These correlations are further reduced by a factor of two when the fire type of the two grid cells is different (forest or savanna).

[34] The diagonal terms $B_{ii}(t)$ of the temporal component of the error covariance matrix are equal to 1. The values of the off-diagonal terms vary linearly between zero for a 6-month interval and 0.5 for successive months.

3.2.3. Correlation Setup for Biogenic Emissions

[35] The error on the biogenic flux parameters is taken equal to 0.6. The spatial correlations between errors on the fluxes emitted by different grid cells depend on the geographical distance between the grid cells and on the distribution of ecosystems [Olson, 1992] used in the biogenic volatile organic compounds (BVOC) emission inventory by Guenther *et al.* [1995]. Let now e_i^n be the fraction of the flux emitted by the grid cell i originating from the ecosystem n . We then define the terms $B_{ij}(r)$ as follows:

$$B_{ij}(r) = \sum_{n,m} C^{nm} e_i^n e_j^m \exp(-d_{ij}/\ell) (\sigma_{\phi_i}/\phi_i) (\sigma_{\phi_j}/\phi_j), \quad (10)$$

where the decorrelation length ℓ is supposed equal to 6000 km. The multiplicative factor C^{nm} is introduced in

order to make out whether the same or different ecosystems occupy the grid cells i and j . In the first case, C^{nm} is equal to 1, and the terms $B_{ij}(r)$ depend only on the geographical distance between the grid cells. When $n \neq m$ in the grid cells i and j , then C^{nm} is taken equal to 0.5.

[36] As for the previous emission categories, the diagonal terms of the temporal part $\mathbf{B}(t)$ of the error covariance matrix are taken equal to 1. A linear decrease from 0.9 to 0.7 is assumed for the off-diagonal terms as the interval between months increases from one (successive months) to six.

[37] In all cases, it has been checked that the resulting error covariance matrix satisfies the desirable property of positive definiteness.

3.3. Big Region Approach: Monthly and Annual

[38] In this approach, the $\Phi_j(x, t)$ of equation (1) are the monthly emissions over large geographical areas for the same broad categories as in the grid-based approach: (1) anthropogenic emissions in 8 regions (Figure 3), (2) forest and savanna burning emissions in 4 regions, and (3) biogenic CO and VOC (isoprene, terpenes, methanol) emissions in 2 regions (Table 2). A total number of 216 flux parameters are quantified by the inversion. The aggregation of fluxes into a few large regions implies that the emission distributions over these regions are assumed to be perfectly known. The diagonal elements of the spatial component of \mathbf{B} , defined as the square of the background errors on the control variables, are given in Table 2. The errors range from 0.35 for sources supposed to be better quantified (i.e., anthropogenic emissions in western Europe, North America, and Oceania) to 0.7 for highly uncertain emission categories (e.g., natural emissions). Temporal correlations are also considered in this approach. The off-diagonal terms of the temporal error covariance matrix \mathbf{B} , corresponding to the errors between the fluxes emitted in different months, are defined in the same way as in the grid-based setup for the different emission categories.

[39] The results of an additional inversion analysis will be also presented, where the seasonality of the sources, provided by the “bottom-up” inventory, is kept constant. In this annual big region inversion, only 18 flux parameters are quantified. The error covariance matrix \mathbf{B} is now diagonal and the prior errors on the control parameters are given in Table 2.

[40] The fact that the number of MOPITT observations is by far greater than the number of parameters to be estimated ensures a quick convergence to the solution. Of the order of 30 iterations are needed to attain convergence in both cases.

4. Results and Discussion

[41] The results of the grid-based and monthly big region inversion studies are presented below. The a priori and optimized CO columns are compared to the MOPITT CO columns for June and December 2000 in Figures 4 and 5, respectively. The optimizations bring the model calculated columns much closer to the measurements at all latitudes, compared to the a priori. Not surprisingly, the model/data bias reduction is larger in the grid-based scheme compared to the big region setup. The geographical distribution of

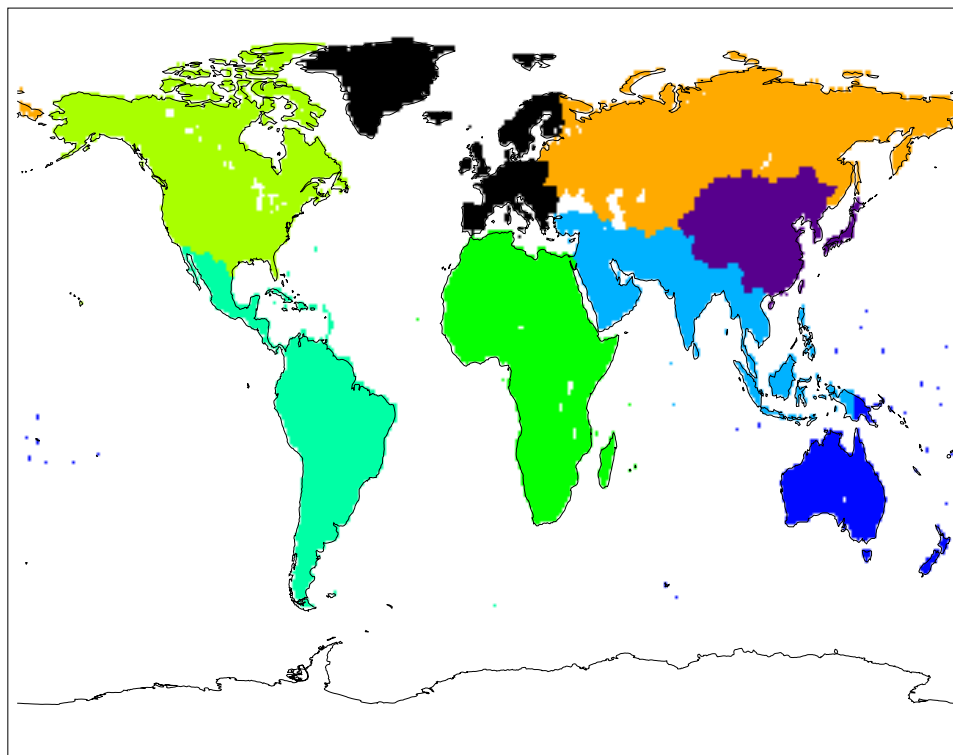


Figure 3. Regions used for the inversion of anthropogenic emissions in the big region approach (Table 2).

the annual emission updates associated to anthropogenic, biomass burning and biogenic sources is illustrated in Figures 6, 7, and 8, respectively. The seasonal variation of the prior and optimized fluxes over several important regions is displayed in Figure 9 (biomass burning), Figure 10 (biogenic), and Figure 11 (anthropogenic). The inversion results by region and emission category are summarized in Table 3.

[42] As seen on Figure 4, the prior modeled columns agree generally well with the data in the Southern Hemisphere, except for an overestimation reaching 70% over Central Africa, whereas they are systematically underestimated by 20 to 30% over the Northern Hemisphere. The increase of the CO columns over the Far East after optimization is mainly achieved by increasing the anthropogenic emissions over this region, by 95% in the monthly big region setup and by 85% on average in the grid-based approach (Figure 6). A significant reduction of the biomass burning emissions over Central Africa is found to be necessary to account for the low observed columns in this region. This reduction is most pronounced in June in southern equatorial Africa, where it reaches a factor of 2 (Figure 9). Despite the lower posterior values of the biomass burning emissions over this region, an overestimation of less than 10% in the grid-based and less than 15% in the monthly big region approach still persists after optimization, however.

[43] In December 2000, the modeled prior columns are in a good agreement with the measurements, except over India, northern Africa, and Brazil, where the discrepancies reach up to 30% (Figure 5). The inversion leads to a significant decrease (35%) of biomass burning emissions

over northern Africa (Figure 9), which is accompanied by a 32% increase of the biogenic emissions in the grid-based scheme (Figure 10), whereas an increase of anthropogenic and biogenic sources by 28 and 17%, respectively, is obtained by the monthly big region solution. To account for the low observed columns over India, anthropogenic emissions over this region are reduced by 30% in both inversions during this month. Furthermore, the increase of the biogenic emissions over South America in December found by both inversions (Figure 10) allows for a better agreement with the MOPITT columns.

Table 2. Control Variables Used in the Big Region Inversion Setup and the Uncertainty Parameters B_{ij} Associated With Them

Control Variables	Regions	$\sqrt{B_{ij}}$
Anthropogenic emissions	North America	0.35
	South America	0.6
	Africa	0.6
	Europe	0.35
	Far East	0.6
	former Soviet Union	0.6
	south Asia	0.6
	Oceania	0.35
	Forest fires: burnt biomass	tropical Asia/Oceania
tropical America		0.7
Africa		0.7
extratropical		0.7
Savanna fires: burnt biomass	North Africa	0.7
	south Africa	0.7
	America	0.7
	Asia-Australia	0.7
Biogenic CO/VOC	tropics	0.7
	extratropics	0.7

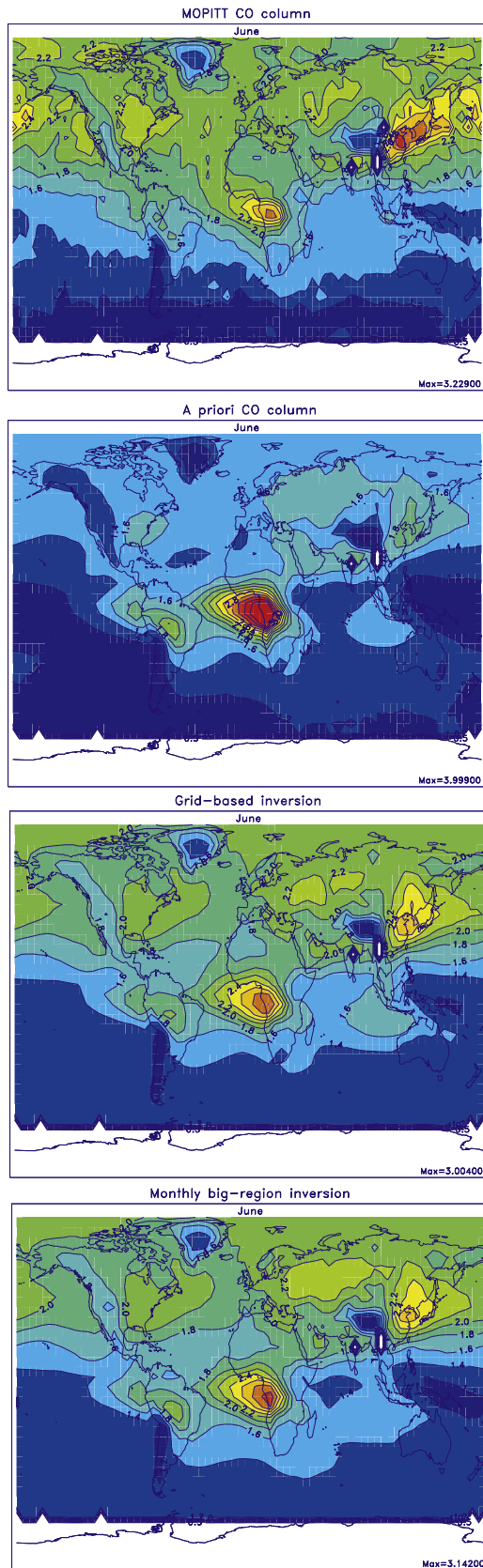


Figure 4. Comparison between the MOPITT, a priori, and optimized columns in June 2000. Units are 10^{18} molecules cm^{-2} .

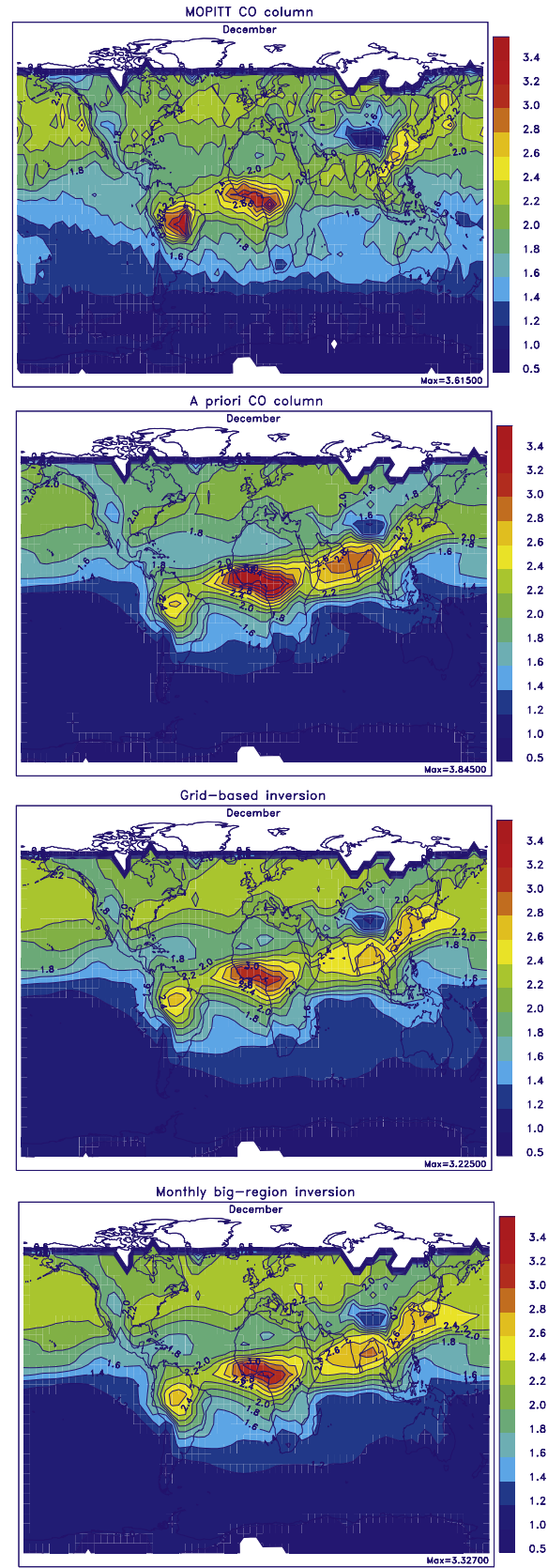


Figure 5. Comparison between the MOPITT, a priori, and optimized columns in December 2000. Units are 10^{18} molecules cm^{-2} .

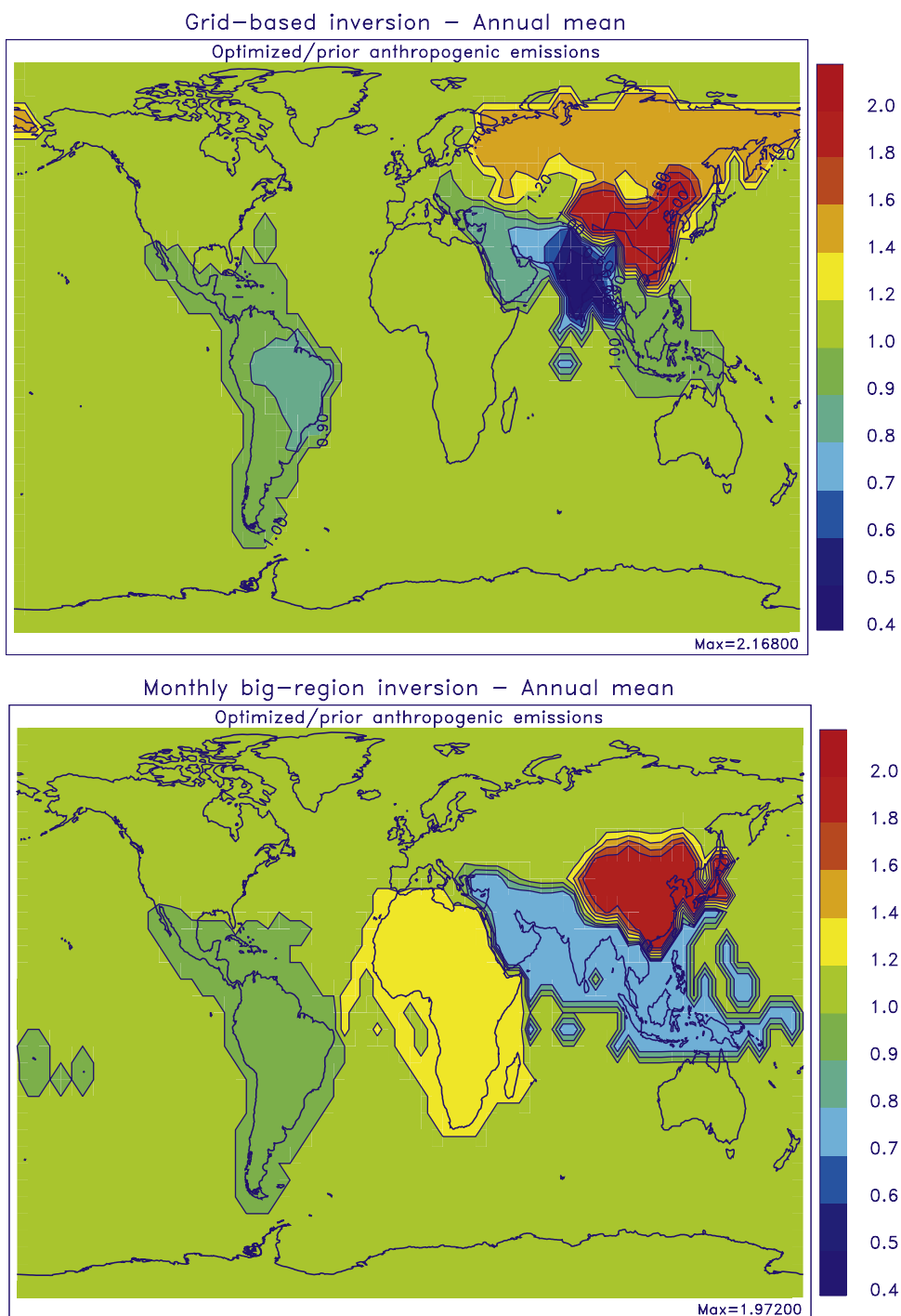


Figure 6. Ratio of optimized to prior anthropogenic emissions estimated by the two inversion methods.

4.1. Summary of Global-Scale Results

[44] Globally, the optimizations point to an increase of the anthropogenic source by about 18%, accompanied by a reduction of the pyrogenic emissions by 7% in the monthly big region and by only 3% in the grid-based scheme. Both inversions agree on enhanced isoprene, terpenes, and methanol fluxes, which are about 15% higher than the prior values. Moreover, the optimized biogenic CO emissions increase by 25% in both analyses. While the photochemical CO production from the oxidation of methane decreases slightly after optimization (Table 1), the NMVOCs oxida-

tion source increases in both cases, by 11 and 8% in the grid-based and the monthly big region setup, respectively. This increase, in combination to the enhanced biogenic CO/VOC emissions, entails an increase of the CO lifetime by 4%. After optimization, the zonally and annually averaged OH concentrations are found to decrease by about 10% in the northern midlatitudes in the model, in response to the increased anthropogenic emissions. Relative changes in OH are often much larger at the regional scales, especially in the upper troposphere, and ranging between -50% (Amazon Basin) and $+70\%$ (Southeast Asia).

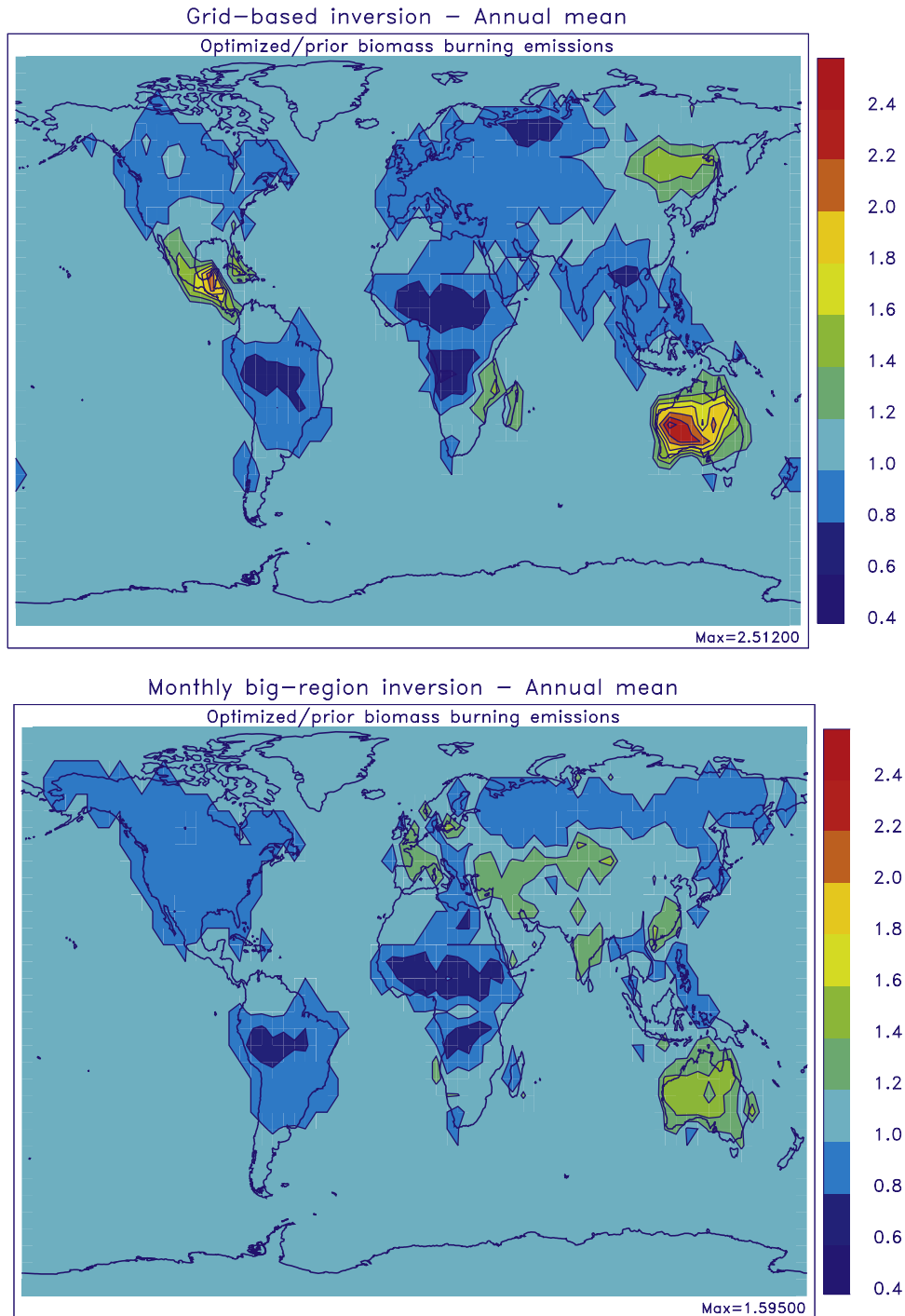


Figure 7. As in Figure 6, but for vegetation fire emissions.

[45] The resulting total CO flux estimates are by 5% higher than the TAR recommended value for the year 2000 amounting to 2760 Tg CO/yr [*Intergovernmental Panel on Climate Change (IPCC)*, 2001], and they compare quite well with the optimized magnitudes in the studies of *Pétron et al.* [2004] (2924 Tg CO/yr) and *Müller and Stavrakou* [2005] (2928 Tg CO/yr). Substantially lower total emissions, ranging from 2363 to 2450 Tg CO/yr, are estimated by *Arellano et al.* [2004]. Part of this disagreement, however, is explained by their pre-

scribed OH fields scaled down by 20%, which implies reduced global CO sources.

[46] Despite the similarities between results of the big region and the grid-based analyses, the high-resolution inversion allows a better exploitation of data, as testified by the larger cost function reduction in the grid-based setup (4.6) compared to the monthly big region one (3.4). The improvement is of the same order (although somewhat smaller) than the improvement resulting from the optimization of the seasonal variation of the emissions: the reduction of the cost in a grid-based analysis where the seasonality of

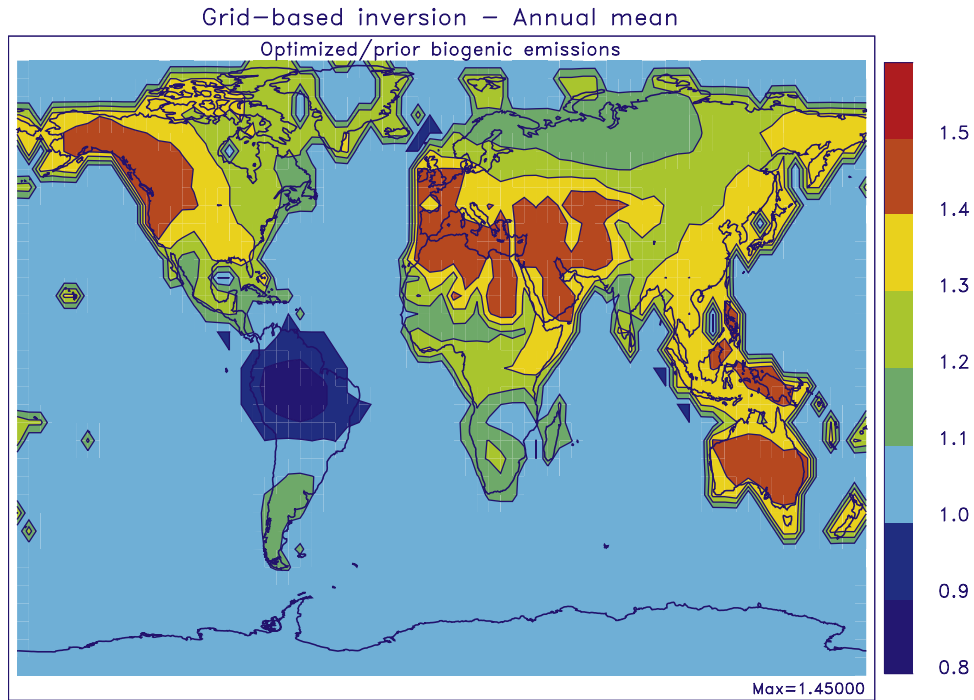


Figure 8. Ratio of optimized to prior biogenic emissions in the grid-based framework.

the emissions is kept unchanged during optimization (results not shown here for brevity) is found to be a factor of 3.1. Finally, when both the seasonal variation and geographical distribution of the emissions within the large regions are kept identical (case of the annual big region inversion), the cost is reduced by a factor of only 2.2 after optimization.

[47] The comparison to independent measurements given in Figures 12 and 13 (for ground-based measurements) and Figure 14 (for aircraft campaigns) shows an overall better model performance after optimization. However, the inversion fails to provide an improvement at the high-latitude CMDL sites of the Southern Hemisphere (e.g., Tierra del Fuego), where an overestimation reaching 30–50% is found during the whole year. The reasons for this discrepancy are unclear. It should be reminded, however, that the inversion is not constrained by MOPITT data poleward of 65°. This overestimation is also found in other global inverse modeling studies performed with different models [e.g., Arellano *et al.*, 2004].

4.2. Anthropogenic Emission Updates

[48] A common feature of both studies is the significant increase of anthropogenic emissions over the Far East, which becomes the largest regional CO emitter, representing about 35% of the global anthropogenic emission. The increase is more pronounced in the grid-based case, peaking at 110% over eastern China, compared to the 97% increase in the monthly big region inversion (Figure 6). Although Arellano *et al.* [2004] and Pétron *et al.* [2004] also estimated an important increase of the east Asian anthropogenic source, their optimized values of 208 and 207 Tg CO/yr, respectively, are 15% lower than our grid-based estimate of 239 Tg CO/yr (Table 3). Our values are also by 25% higher compared to Palmer *et al.* [2003] and Heald *et al.* [2004]. Further, the grid-based analysis provides higher east Asian anthropogenic emissions in

winter and springtime, peaking in March (green line, Figure 11). This result is very similar to that obtained by the inversion study of Pétron *et al.* [2002], where the higher values of the Asian flux occur also in March.

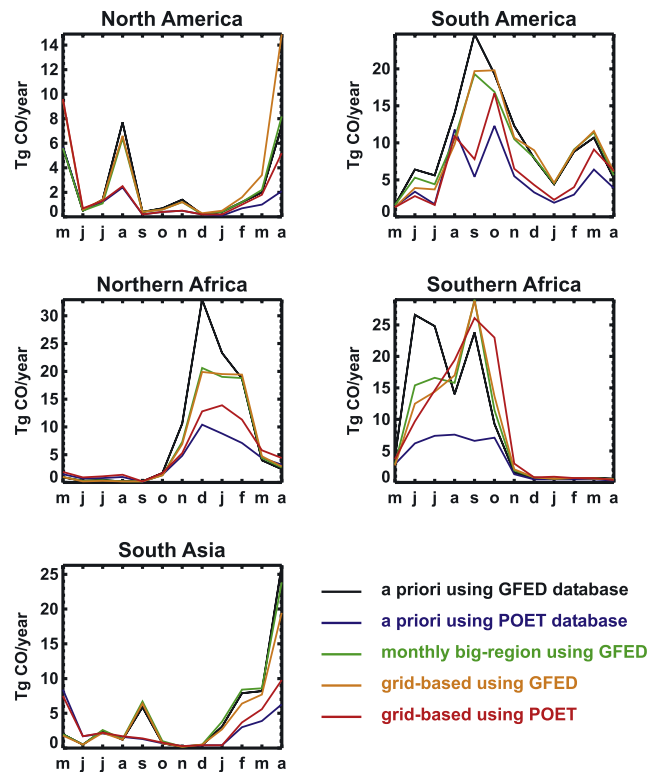


Figure 9. Seasonal variation of the biomass burning emissions by region as estimated by inversion studies conducted using the GFED database [Van der Werf *et al.*, 2003] and the POET database [Olivier *et al.*, 2003].

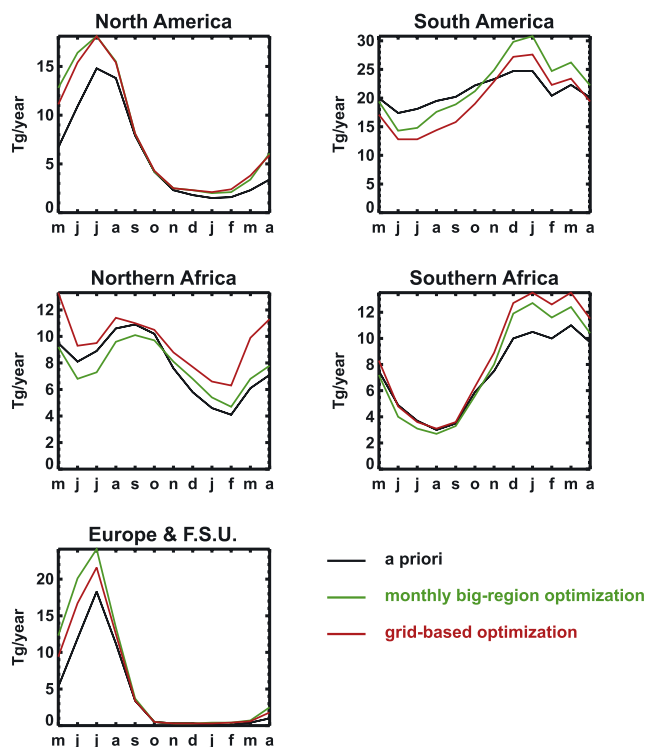


Figure 10. Comparison between prior and optimized monthly biogenic VOC (isoprene and terpenes) emissions by region.

[49] The discrepancies between our emission estimates and previous studies might be related to the treatment of transport processes in the model, e.g., to an underestimation of vertical mixing above this region. The underestimation of the modeled abundances over the northern Pacific between February and April shown in Figure 13 (Mauna Loa, Midway, also MOPITT over the northeastern Pacific) points to either insufficient transport from east Asia during wintertime (which might be partly related to vertical mixing over these areas) or, even more, to overestimated OH abundances in (late) winter. Both potential biases could lead to excessive posterior emissions over the Far East, given the relatively low sensitivity of the MOPITT retrievals to the boundary layer. Another possible cause for differences between the results of different inversion studies lies in the prior emissions used. We note, for example, that the studies of *Palmer et al.* [2003] and *Heald et al.* [2004], which used lower prior emissions over east Asia (115 Tg/yr, i.e., 12% lower than in EDGAR3) provide also the lowest posterior estimates.

[50] Comparison between the prior and optimized mixing ratios with in situ monthly averaged measurements at two Japanese sites provided by the World Data Centre for Greenhouse Gases (*Tsutsumi et al.* [2005], <http://gaw.kishou.go.jp/wdceg.html>) shows a substantial improvement at Ryori (located in the northern part of the Honshu island), except for a persistent underestimation in spring and summertime (Figure 12). At Yonagunijima, the westernmost Japanese island (24.5°N, 123°E), located at no more than 700 km away from mainland China, the optimization fails to reproduce the observations, especially in wintertime, the discrepancy peaking at about 70 ppb in January and

February. This overestimation is probably related to the steep gradients encountered in this region in winter (predicted mixing ratios higher than 400 ppbv over mainland China, more than a factor of 2 higher than in the vicinity of Yonagunijima) and to the relatively coarse resolution of the model, as indicated by the satisfactory agreement between the data and the optimized model mixing ratios at 125°E, 2 degrees eastward from the station location (dashed line on Figure 12), suggesting that either the horizontal interpolation applied to the model values is not reliable at this site, or that the continental mixing ratios are overestimated by the model during the winter. This interpretation is supported by the comparison results at the Tae-ahn NOAA CMDL station, situated in the Korean Peninsula. Although the inversion performs quite well during springtime, a substantial overestimation takes place in wintertime, as shown in Figure 13. This disagreement might partly be related to the vicinity of the source regions and to a possible underestimation of vertical mixing in wintertime in this region.

[51] The inversion results over east Asia are further evaluated against CO mixing ratio profiles measured during the Transport and Chemical Evolution over the Pacific (TRACE-P) aircraft campaign conducted in February–April 2001 (http://www-gte.larc.nasa.gov/gte_miss.htm). Note that importance should be attached only to the general features of this comparison, since biases are expected due to the fact that we compare modeled values representing monthly averages with data obtained at various specific times. For our purposes, these observations are averaged over large regions (Figure 14). As illustrated in Figure 14, the optimization succeeds quite well in bringing the model much closer to the observations over the North Pacific and the China Sea. This is reflected in the lower-than-unity

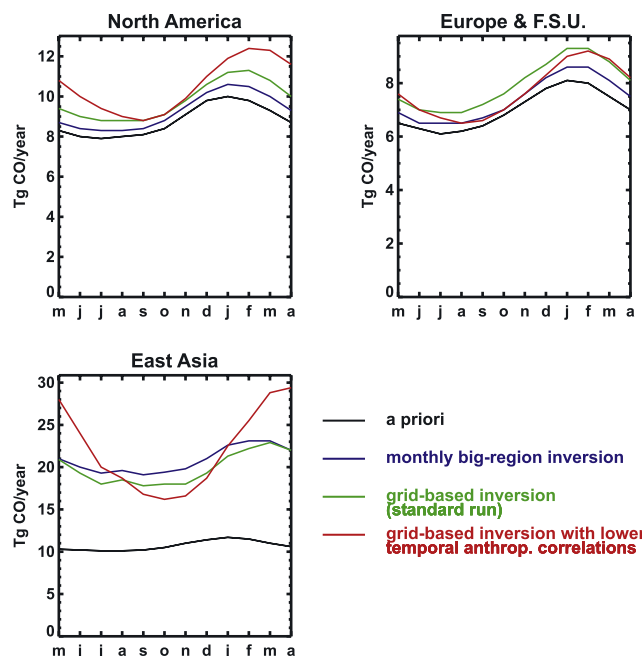


Figure 11. Seasonal variations of the anthropogenic emissions by region estimated by the big region and grid-based (standard) inversion, as well as by a sensitivity test conducted using lower values for the temporal anthropogenic correlations (red line).

Table 3. Inversion Results by Region and Emission Category^a

Source Category	Regions	A Priori	Grid Based	Big Region Monthly	Big Region Annual
Anthropogenic emissions, Tg CO/yr	North America	90	103	97	93
	South America	40	37	38	40
	Africa	76	82	102	101
	Europe	47	47	47	50
	Far East	129	239	253	233
	former Soviet Union	38	48	41	63
	south Asia	146	103	102	90
	Oceania	5	5	5	5
Tropical forest fires, Tg CO/yr	Asia/Ocean	51	44	48	52
	America	88	88	77	63
	Africa	31	30	34	55
Savanna fires, Tg CO/yr	Asia-Australia	44	62	61	80
	America	52	54	50	43
	Africa	172	141	138	91
Isoprene and terpene emissions, Tg/yr	Asia	150	201	166	171
	Africa	181	218	185	200
	America	324	326	358	366
	Europe	17	23	26	21
	Oceania	40	56	45	45

^aNote that for the biogenic emissions, Europe includes also the European part of the former Soviet Union.

ratios of the root mean square relative deviations of the optimized simulations by the corresponding a priori values (0.54 for the North Pacific and 0.60 for the China Sea region). The quality of the inversion, however, worsens in the north tropical Pacific, where the model fails to reproduce the observed negative gradient in CO mixing ratio between the lower and the upper troposphere.

[52] Another common feature of both inversions is the reduction of the south Asian anthropogenic emissions by 30% (Table 3). This result is in disagreement with previous big region inversion studies, which call for an increase of the south Asian emissions by 12% from *Pétron et al.* [2004], and by 75% from *Arellano et al.* [2004]. Although the reasons for these discrepancies are unclear, they are probably related to differences in the inversion approaches as well as to intermodel differences in this region, in particular during the winter, when the IMAGES model overestimates the CO columns even with reduced anthropogenic emissions. We have explored the possibility that the screening effect of aerosols on the MOPITT measured columns could explain the model/data bias. High aerosol optical depth (AOD) values at 500 nm have been recently reported by *Dey et al.* [2004] at the AERONET north Indian Kanpur station in May and June, mostly due to dust storms which are common in India in this period. Values as high as about 1 in this region are also confirmed by the AOD estimated from the Total Ozone Mapping Spectrometer (TOMS) fields [*Torres et al.*, 1998]. In contrast to the significant reduction of the AOD associated to small particles (e.g., sulphate) between the visible and the infrared, the AOD associated to the relatively large dust particles shows little variation when moving from the visible range to higher wavelengths [*Takemura et al.*, 2002]. Since the MOPITT instrument is operated in the infrared (at 4.7 μm) and the CO retrievals don't take the possible effects of aerosols into account, they may be perturbed by aerosols from dust storm events over the Indian subcontinent, which therefore introduce a possible underestimation of the observed columns. This conclusion is not supported by the analysis of the IMAGES/MOPITT biases over India, how-

ever, since they don't exhibit higher values during the dust storm season.

[53] The estimated decrease in south Asian anthropogenic emission estimates is supported by the study of *Heald et al.* [2004] which estimates a factor of 2 decrease in Indian emissions, as well as by the comparison of the modeled mixing ratios with CO measured at the Kaashidhoo Climate Observatory of Maldives (northern Indian Ocean) between February 1998 and March 2000 [*Lobert and Harris*, 2002] shown on Figure 12. The inversion analysis is seen to provide a significant improvement during the dry season, although an overestimation, reaching 30% in February, still remains. A similar overestimation is also found in the optimized columns during this month over the Maldives, which are by 15% higher than the MOPITT observed

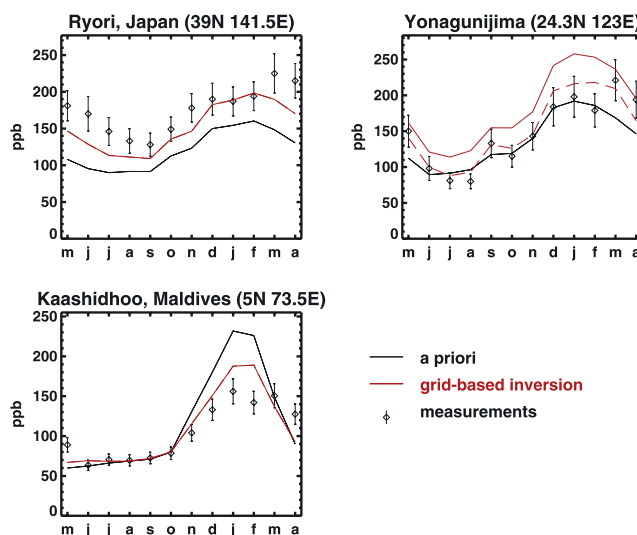
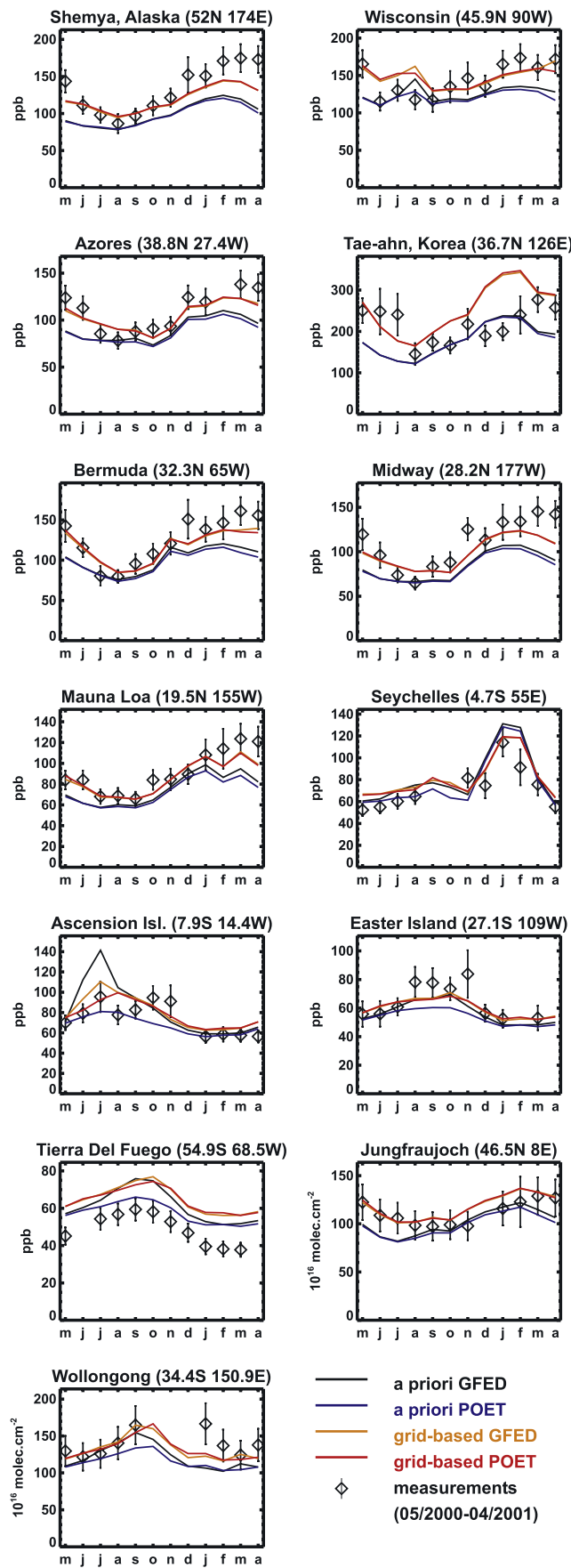


Figure 12. Comparison between a priori, optimized, and observed monthly averaged CO mixing ratios at two Japanese stations and one Indian Ocean station. The dashed line represents the optimized model values calculated at 125°E, 2 degrees eastward from the station location.



columns. Further comparison of our results with CO measured at the Seychelles NOAA CMDL station shows an overall good agreement and a greater bias reduction in the dry season, the optimized values at this site being affected by the estimated decrease of the south Asian emission strengths (Figure 13).

[54] As seen on Figure 6 and Table 3, small changes in anthropogenic emissions over North and South America, Europe and Oceania are obtained by both inversions. Over Africa, the monthly big region result calls for an increase of the anthropogenic emission estimate by 35%, whereas the grid-based optimized fluxes stay very close to their prior values. This difference should be considered in relationship with the optimization of the biogenic CO and VOC emissions. In fact, only a slight increase of the African biogenic fluxes is estimated by the monthly big region inversion (Figure 10 and Table 3), whereas the grid-based solution suggests a larger increase, especially over the northern part of Africa (Figure 8). This result reflects the relatively limited skills of the monthly big region scheme, which counts only 2×12 parameters for this source globally (Table 2). In contrast, the large number of control parameters in the grid-based approach allow potentially important emission changes in order to capture the fine features of the data and provide satisfactory emission distribution patterns. Note that the African anthropogenic strengths derived by our grid-based analysis are in good agreement with the IPCC [2001] and the Müller and Stavrou [2005] estimates (82 against 80 and 85 Tg CO/yr).

[55] The anthropogenic emissions over the Former Soviet Union are higher in the grid-based inversion study, 48 Tg CO/yr against 41 Tg CO/yr in the monthly big region approach (see Table 3 and Figure 11). Comparison of our results to previous inversion studies [Pétron et al., 2004; Arellano et al., 2004] constrained by MOPITT data shows that their flux estimates are close to the prior, and very similar to our grid-based values over this region. The inversion results of Pétron et al. [2002] and Müller and Stavrou [2005] based on CMDL data and the IMAGES model suggest, however, an important increase of emissions, in agreement with the results of the annual big region sensitivity study shown in Table 3. The increase could be the consequence of an inadequate description of the emissions by the control parameters over this region in the annual big region scheme. After optimization, the reduction of the MOPITT/model bias is larger in the grid-based than in the big region solution. Evaluation of the results against CO mixing ratios measured at the Shemya and the Mauna Loa NOAA CMDL stations (Figure 13) shows that both inversions perform quite well during the whole year, influenced by the increased emissions over north Asia. Nevertheless, the remaining underestimation of about 30 ppb at Shemya in springtime is consistent with the positive model/MOPITT data bias of about 15% found over Russia in wintertime.

Figure 13. Comparison between a priori, optimized, and observed monthly averaged CO mixing ratios at selected CMDL and column-measuring stations.

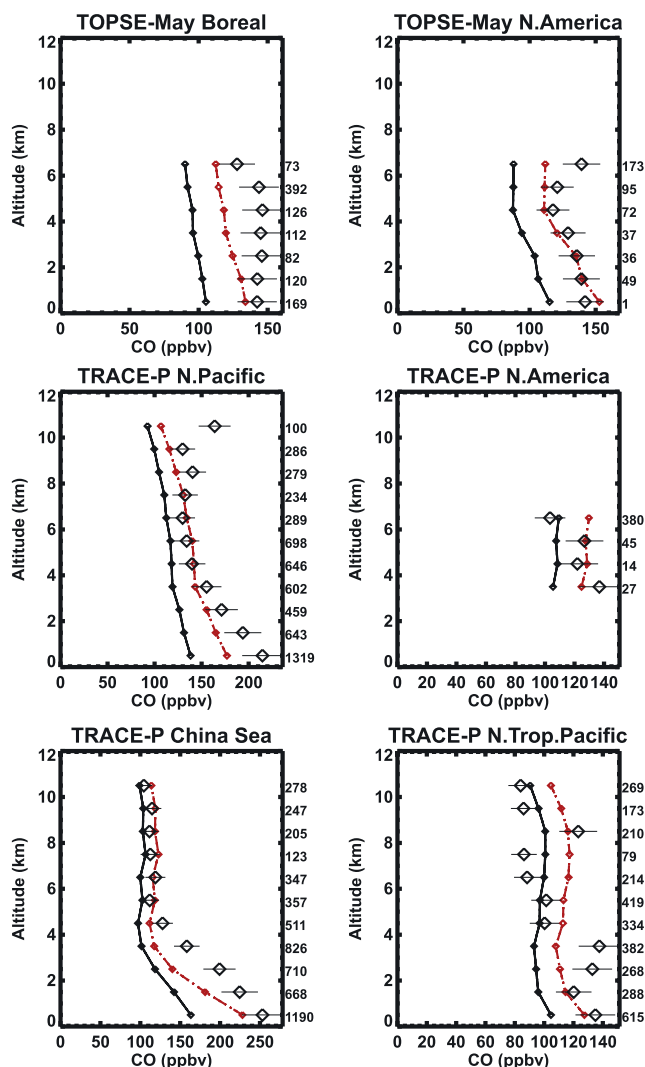


Figure 14. Comparison of CO mixing ratios from the TOPSE and TRACE-P aircraft campaigns averaged over large regions and optimization results using the grid-based (red line) approach. A priori values are in black. The separation line between the North Pacific and the north tropical Pacific is set at 25°N, and both regions extend eastward from 130°E, while the China Sea region extends westward from 130°E. The numbers on the right of each plot represent the number of measurements taken into account at the corresponding altitude. The error bars represent standard deviations of the data.

4.3. Pyrogenic Emission Updates

[56] A result common to both inversions is the decrease of the African savanna burning emissions, reaching 18% and 20% in the grid-based and the monthly big region setup, with respect to the prior GFED inventory (Table 3 and Figure 7). Regarding the African forest fire emissions, slight changes are found after optimization. The African vegetation fire emissions, amounting to 203 Tg CO/yr in the prior, are reduced to about 172 Tg CO/yr in both solutions and are therefore in good agreement with the corresponding a posteriori best estimate by *Arellano et al.* [2004] amounting to 153 Tg CO/yr.

[57] The spatial and temporal correlations applied to the vegetation fire emissions provide a relative homogeneity on the inferred emission changes over Africa, even though the emission patterns vary considerably between seasons. As illustrated in Figure 9, the high prior GFED values from November to March over northern Africa, peaking at 33 Tg CO/yr in December, as well as the maximum value of 27 Tg CO/yr taking place in June over southern Africa are significantly reduced by both inversions (green and orange lines).

[58] To check whether our results depend on the prior biomass burning inventory used, we conducted a sensitivity study using the POET database [*Olivier et al.*, 2003], while keeping the same background errors. Although the two inventories differ substantially over Africa, as shown by the black and blue lines of Figure 9, the POET estimates being generally much lower, the grid-based results exhibit an excellent convergence both in seasonality and in emission magnitudes over this region. In particular, the GFED peak over southern Africa in June (about 27 Tg CO) is not confirmed by the posterior results, which call for an emission of 12.5 Tg CO in the grid-based case, approaching the posterior estimate of 9.7 Tg CO using the POET database. On the other hand, the September peak in the GFED inventory is supported by both grid-based inversions: it is preserved in the GFED optimization (28.8 Tg CO), and found to be required by the sensitivity inversion (27 Tg CO/yr), although the prior POET values are very low (6.6 Tg CO). Because of the decrease of the south African biomass burning source from June to August, all inversion studies lead to a large bias reduction at the NOAA CMDL Ascension station during the same period (Figure 13). Note here that the posterior biomass burning emission estimates based on GFED and POET differ substantially in regions other than Africa. This is partly due to the collocation of pyrogenic sources with strong anthropogenic and/or biogenic sources, which makes difficult for the inversion to distinguish between different emission categories.

[59] The grid-based optimization estimates a doubling of the North American biomass burning emissions (including Central America) in springtime, which is not reproduced in the monthly big region scheme, as illustrated in Figure 9. These enhanced flux estimates, however, contribute to the more significant bias reduction achieved at the NOAA CMDL Bermuda station during this season (Figure 13). On the other hand, due to the high posterior emissions in August over North America, the inversion falls short of reducing the bias at the NOAA CMDL Wisconsin station during this month.

4.4. Biogenic Emission Updates

[60] A global increase of biogenic CO and VOC emissions is found by both inversion solutions. This increase reaches about 15% for isoprene/terpenes and 24% for biogenic CO in the grid-based framework, whereas it is somewhat less significant in the monthly big region approach, as seen in Table 1. These findings are, however, in disagreement with previous inversion studies, which estimated decreased posterior biogenic emissions [*Arellano et al.*, 2004; *Müller and Stavrou,* 2005]. As results from Figure 8 and Table 3, the largest biogenic emissions

Table 4. Error Reductions Calculated by Region and Emission Category for the Grid-Based Inversion Scheme

Regions	Anthropogenic	Pyrogenic	Biogenic
North America	1.2	1	1.5
South America	1	1.2	2.3
North Africa	1.1	1.1	2
South Africa	1.1	2.3	2.1
Europe	1.2	1.1	1.9
Far East	1.7	1	1.7
Former Soviet Union	1.3	1	2.4
South Asia	1.3	1.1	2
Oceania	1	1	1.6
Tropics(25°N–25°S)	1.3	1.4	3.9
Extratropics	1.8	1	2.7

increases are found over Oceania, over the western North America and around the Mediterranean basin, whereas an important reduction of the flux estimates is obtained over the northern part of South America, especially in June and July. The latter finding is in qualitative agreement with field studies indicating that isoprene emissions are overestimated by the GEIA inventory of *Guenther et al.* [1995] in large parts of Amazonia, in particular during the wet season [*Helmig et al.*, 1998; *Rinne et al.*, 2002; *Trostdorf et al.*, 2004]. In the midlatitudes of the Northern Hemisphere biogenic emissions are increased in all seasons, but particularly in spring and summertime (Figure 10). Comparison between the inversion-derived CO mixing ratios with Tropospheric Ozone Production about the Spring Equinox (TOPSE) aircraft campaign measurements conducted in 2000 (<http://topse.acd.ucar.edu>) over the high and midlatitude continental North America during the winter-spring transition, shows a good agreement, partly due to the large biogenic fluxes estimated over this region (Figure 14). Many factors are believed to influence the seasonality of the BVOC emissions, like the leaf age, the water status of the soil and canopy [*Trostdorf et al.*, 2004; *Plaza et al.*, 2005] and the environmental conditions (temperature and light) encountered in the past hours and days [*Kuhn et al.*, 2004; *Guenther et al.*, 1999]. Besides these factors, observations suggest a strong dependence of the basal emissions on leaf age for the monoterpenes [*Staudt et al.*, 2004; *Tarvainen et al.*, 2005; *Holzinger et al.*, 2005] and methanol [*McDonald and Fall*, 1993; *Jacob et al.*, 2005], which is not accounted for in the prior inventory. More specifically, the emissions of methanol and monoterpenes appear to be often enhanced in spring, and depleted in autumn as a result of senescence. Although we do not know whether these effects explain the changes estimated by our inversion for biogenic

emissions, they clearly suggest that large uncertainties are attached to their seasonality.

4.5. A Posteriori Uncertainties

[61] In order to calculate the posterior errors, we apply an off-line iterative approximation of the true inverse Hessian matrix using the Davidon-Fletcher-Powell (DFP) updating formula [e.g., *Nocedal and Wright*, 1999], as explained by *Müller and Stavrou* [2005]. For this purpose, the background error covariance matrix **B** of equation (3) is used in combination with the most recently acquired information by each iteration of the minimization procedure. The posterior error covariance matrix of the control variables is calculated as the inverse Hessian of the cost function at its minimum, and the square root of its diagonal elements are the standard errors associated to the optimized parameter vector. The errors on the emissions in the grid-based scheme have been computed over large continental regions. The error reduction, i.e., the ratio of the priori by the a posteriori error, is calculated by region and by emission category and is presented in Table 4.

[62] In all cases, the posterior errors are smaller than the a priori estimates. Of all sources, the uncertainty for biogenic sources decreases the most. As shown in Table 4, the error reduction is more pronounced in the tropics (factor of 3.9) than in nontropical regions (2.7). Error reductions greater than 2 are also found over the Former Soviet Union (2.4), South America (2.3), and Africa (2.1). Regarding the anthropogenic sources, the largest error reduction is achieved over Far East (1.7), as well as over south Asia and the Former Soviet Union (1.3). The posterior errors on anthropogenic emissions over regions with low prior uncertainties, like Europe, North America and Oceania, remain quite close to their initial values. Regarding the vegetation fire emissions, the most significant error reduction is obtained over southern Africa (2.3), whereas the posterior error estimates for other regions remain close to their prior values.

[63] Generally, after optimization, the strongest sources happen also to be the best constrained ones. Note that the error reductions calculated in the big region analyses (not shown here for the sake of simplicity) are found to be systematically larger than in the grid-based setup. For example, tropical biogenic emission errors are reduced by as much as a factor of 7.9 in the annual big region inversion, and anthropogenic emission errors over the Far East are reduced by a factor of 2.5. The higher reductions found by the big region scheme are a consequence of its limited resolution. Given the small number of control parameters

Table 5. Results of Different Sensitivity Studies^a

Sensitivity Inversions Performed	Anthropogenic Fluxes	Tropical Fires	Savanna Fires	Extratropics Fires	Biogenic Fluxes	Photochemical Source	Total
Prior	571	170	268	29	160	1530	2748
S0, standard grid-based	664	162	257	31	199	1574	2907
S1, errors on control variables doubled	620	144	268	27	221	1600	2900
S2, errors on control variables halved	672	170	262	32	185	1556	2897
S3, decorrelation lengths doubled	667	161	258	29	202	1592	2909
S4, decorrelation lengths halved	677	166	257	32	192	1570	2914
S5, varying temporal anthropogenic correlation	705	156	250	29	193	1567	2920
S6, anthropogenic correlations halved	653	163	257	31	200	1576	2900
S7, constant biogenic fluxes	760	187	260	43	160	1532	2942

^aThe total estimates include also the oceanic CO source amounting to 20 Tg CO/yr.

and the assumption that the geographical distribution of the emissions within the large regions (as well as their seasonal variation in the annual inversion analysis) are perfectly known in this setup, the range over which these parameters may change in order to get the constraints satisfied is small, and the resulting posterior uncertainties are necessarily low. The error reduction of the grid-based setup should be considered as more realistic, since they better reflect uncertainties in the seasonal variation and fine-scale distribution of the prior emissions.

5. Sensitivity Studies

[64] A number of sensitivity tests have been carried out to assess the influence of various parameters on the inferred fluxes. All tests have been performed with the grid-based inversion scheme. To investigate the impact of the assigned a priori uncertainties on the control variables, we carried out two inversion experiments where the background errors are doubled (S1) or halved (S2, Table 5). Doubling or halving the decorrelation length scales used for the biomass burning and biogenic emissions is studied in the S3 and S4 tests, respectively. Further, the sensitivity of the results to the assumed anthropogenic error correlations is also examined, with a simulation using lower temporal correlations (S5), and a simulation with halved spatial correlations (S6). In S7 experiment, biogenic CO and VOC emissions are fixed and we optimize only for CO direct sources. The results of these tests are summarized in Table 5 and are discussed below. Note that the percentages reported in this section concern comparisons of the sensitivity inversions with the standard grid-based simulation (S0), unless otherwise stated.

5.1. Background Errors Halved or Doubled

[65] As expected, the standard grid-based optimization S0 fluxes for the different emission categories fall generally within the range of the estimated fluxes of the S1 and S2 tests. When the background errors on the control parameters are doubled, the biogenic CO and VOC emissions undergo the most significant changes, increasing by 15% over Africa and Asia, while decreasing by 20% over South America. Globally, the biogenic CO source and the isoprene/terpenes fluxes increase by 11% and 8%, respectively. The anthropogenic emissions over South America and south Asia are reduced by 40% and 20% in the S1 scenario, whereas they increase by 8% and 18% in the S2 case study. The remainder of the sources, however, is found to be less sensitive to the changes of errors in these two experiments. As expected, convergence is more rapidly attained in the S2 optimization (about 30 iterations) compared to the S1 scenario (100 iterations). Due to the strong confidence granted to the prior information in the S2 experiment, the cost is reduced by only a factor of 3.1. This value is much lower than the value of 4.6 obtained in the standard inversion. The only slightly better cost reduction (factor of 5.1) obtained in inversion S1 indicate that the choice of the background errors in S0 was appropriate.

5.2. Decorrelation Lengths Halved or Doubled

[66] Very weak sensitivity of the global emission estimates is found when doubling or halving the decorrelation lengths for the biomass burning and the biogenic emissions.

Dividing the error decorrelation scale by two leads to decreased biogenic emissions over the Northern Hemisphere (by 4% in North America, by 8% in Europe, by 5% over Asia) and to increased tropical forest fire emissions, especially over North America (12%). A slight increase of anthropogenic emissions is found in the S4 scenario, on the order of 9% over Russia and 4% over Europe, compared to the S0 analysis. Doubling or halving the error correlation scales results, however, in deteriorating the inversion performance, as indicated from the lower cost reductions obtained (3.7 and 3.5 in S3 and S4), especially in the S4 scenario, compared to the standard grid-based simulation. When the error correlation length is decreased, less information is propagated from strong emitting regions to adjacent, weakly emitting areas, which are less directly constrained by the observations. As a result, regions with high fluxes are overly solicited by the optimization in order to fit the observations, whereas regions with low emission strengths show systematically lower emission updates. The quality of the inversion is expected to worsen further in the extreme scenario where the decorrelation length becomes comparable to the model length scale.

5.3. Varying Error Correlation Setup for Anthropogenic Emissions

[67] Two additional experiments have been performed to evaluate the importance of the assumed anthropogenic spatiotemporal error correlations on the posterior estimated fluxes. In the S5 inversion setup, the temporal correlations decrease linearly between 0.9 for successive months and 0.8 for a 6-month interval. As illustrated in Figure 11, this setup leads to a more pronounced seasonal cycle of anthropogenic emissions over North America and east Asia. The peak-to-trough differences become larger over both regions, and they amount to as much as 50% of the annually averaged flux over east Asia. In addition, the maximum and minimum values are shifted by one month over east Asia. An overall increase of 8 and 11% is estimated for the North American and east Asian anthropogenic emissions, respectively, whereas the global anthropogenic emissions are increased by 6%. Other sources, however, exhibit very weak sensitivity to the assumed correlations. Comparison of the optimized concentrations with the NOAA CMDL measurements shows, however, a bias increase over east Asia, especially at the Tae-ahn station in springtime, but a better agreement with the North American stations in the same season.

[68] The estimated fluxes exhibit a very weak response to the change in the error correlation setup of the S6 optimization, except for the east and south Asian anthropogenic fluxes which are increased and decreased, respectively, by 9% with respect to the standard optimization. Lowering the spatial anthropogenic error correlations between fluxes amounts to assuming that the geographical distribution of the emissions within one country and between countries belonging to the same world zone is less well known. As expected, this assumption leads to more contrasted emission distribution patterns, compared to the standard optimization. The performance of the inversion worsens slightly in this experiment, as shown by the lower computed cost reduction compared to the S0 simulation.

[69] Overall, these sensitivity studies show that the inversions yield quite robust results, being not strongly depen-

dent on the choice of the a priori uncertainties and spatio-temporal correlations. It is also worth noting that the discrepancies between the observed and the optimized columns increase in almost all sensitivity inversions.

5.4. Fixed Biogenic VOC Emissions

[70] In contrast, keeping the biogenic CO and VOC sources constant (experiment S7) leads to important adjustments of the anthropogenic and pyrogenic flux estimates. The extratropical forest fire source increases by 40%, accompanied by a 15% increase of the anthropogenic and tropical forest fire source. The analysis does not succeed in reducing the model/data biases in all regions, in particular in springtime over biomass burning areas of the Northern Hemisphere (Central America and eastern Siberia), where the model columns are largely overestimated. The biogenic emissions being held constant, large biomass burning emission increases are required to reduce the model/data bias during spring, leading to these overestimations over the source regions. Generally, the inversion performs poorly in this case, as demonstrated by the 20% lower cost reduction achieved. Further, our global total estimate in this experiment is found to be in excellent agreement with the best estimate of *Pétron et al.* [2004], amounting to 2924 Tg CO/yr, although our totals for anthropogenic and biomass burning emissions are higher by 11 and 20%, respectively. Note that in the work by *Pétron et al.* [2004], biogenic VOC emissions are also not subject to optimization.

6. Conclusions

[71] We have presented and compared two inverse modeling frameworks based on the adjoint of the global chemistry transport model IMAGES. They have been used in order to provide improved source estimates for three categories, namely, anthropogenic, biomass burning and biogenic emissions, based on the MOPITT CO columns retrievals from May 2000 to April 2001.

[72] In the big region inversion scheme, the monthly emissions of CO and biogenic VOC are optimized over large geographical regions, while their spatial distribution within these regions are kept constant. In contrast, the grid-based inversion method is performed at the resolution of the model ($5^\circ \times 5^\circ$). To reduce the underdeterminacy due to the large number of unknowns to be adjusted in this case, we assign spatiotemporal correlations among prior errors on the control parameters. In the case of anthropogenic emissions, it is supposed that the errors on the fluxes are highly correlated within the same country, weakly correlated within large world zones, and uncorrelated otherwise. As for the vegetation fire and biogenic emissions, we assumed that the spatial correlations decrease exponentially with the geographical distance, and are further reduced when the fire or ecosystem type differs.

[73] An additional feature of the proposed inversions is the simultaneous optimization of the sources of the main biogenic VOC compounds (isoprene, terpenes, and methanol), whose oxidation constitutes the major part in the photochemical CO production due to the NMVOCs. The adjoint-based framework allows the inversion to account for the interdependence of CO and the NMVOCs through the chemistry of the hydroxyl radical (OH), and therefore to

constrain the indirect CO source in a fully consistent manner.

[74] The inversion-derived global annual flux of CO amounts to 2900 Tg CO/yr in both the grid-based and the monthly big region setups. This is by 5% higher than the first guess of 2748 Tg CO/yr for the target period from May 2000 to April 2001. The top-down direct CO emission estimates increased by 7%, due to an increase of anthropogenic sources by 18% with respect to the prior. The largest anthropogenic increases are found over east Asia (85% in the grid-based, 95% in the monthly big region scheme) and the Former Soviet Union (26% in the grid-based), whereas changes of less than 15% are found over Europe, America and Oceania. A significant reduction is obtained, however, for the south Asian anthropogenic source, reaching 30% in both schemes compared to the prior. The magnitude of the biomass burning CO emissions also decreased in both simulations. In particular, the African savanna fire source strength is reduced by about 18%. A finding common to the two setups is the enhancement of the biogenic VOC flux estimate, which is found to be about 15% higher than the prior on the global scale in the grid-based solution. This result leads to a 10% increase of the NMVOCs oxidation source. Despite the slight decrease of the methane oxidation source, the total indirect CO source is enhanced by 2–3%.

[75] Both inversion methods succeed quite well in reducing the model/MOPITT data biases over all latitudes. The improvement is more significant in the grid-based analysis, as shows the higher reduction in the cost function (4.6 against 3.4 in the monthly big region approach). Although the magnitudes of the estimated fluxes are similar in the two setups on the global scale, the grid-based derived emission patterns are likely to be more realistic, because they better reflect the uncertainties in the fine-scale distribution of the emissions. Our inversion results have been evaluated against surface observations as well as air-based measurements. Both optimization methods lead to significant improvements in the model performance. However, the comparisons point to possible model flaws, e.g., a possible underestimation of vertical mixing in east Asia in winter-time, or an overestimation of OH abundances at midlatitudes during this season. The impact of the model errors on the inversion results is difficult to assess, although it is expected to be important, as witnessed, e.g., by the significant differences between the results of the different CO inversion studies based on MOPITT phase 1 data. Since the inversion methodology and setup (i.e., choice of control parameters, prior errors and correlations, treatment of the indirect CO source and of chemical feedbacks, etc.) are likely to play a large role as well, there is a clear need for comparison studies involving several models, in order to clarify the respective role of inversion assumptions and model differences on the optimization results.

[76] The errors on the control variables after optimization are computed using an approximation based on the DFP formula. The most significant error reductions concern the biogenic emissions in the tropics, the Asian anthropogenic emissions, as well as the vegetation fire source over the northern and southern Africa. Other sources turn out to be poorly constrained, in particular the anthropogenic sources over industrialized countries. In general, the calculated

uncertainties are lower in the monthly big region setup compared to the grid-based solution.

[77] The sensitivity of the posterior emissions estimates to a number of assumptions, such as the a priori uncertainties and the assumed spatiotemporal correlations has been investigated. The global CO budget shows little sensitivity to the background errors, whereas regional emission estimates are more affected. The overall MOPITT/model bias is significantly less reduced when these errors are halved, however, whereas only a small improvement is found when they are doubled. Little sensitivity of the results is found when we double or half the error length scale applied for biomass burning and biogenic emissions. Opting for lower temporal correlations on anthropogenic emission errors leads to a higher amplitude of the seasonal cycle of emissions over North America and the Far East. Moreover, in order to assess the influence of the prior biomass burning inventory, we conducted an additional sensitivity simulation using the POET biomass burning emissions inventory. The posterior biomass burning seasonal cycles for the two simulations are found to converge remarkably well over Africa, in spite of the relatively large discrepancies between the prior inventories. Overall, the inferred estimated emissions are found to be quite robust to different setups, with regional emission estimates differing by less than 10%. Differences between regional emission estimates by the grid-based and monthly big region approaches are somewhat larger, on the order of 20% (see Table 3).

[78] This study proves the feasibility and skills of the high resolution grid-based technique for deriving improved flux estimates for a reactive species at the global scale. The spatial and temporal correlations between errors on the fluxes prove to be essential in order to better constrain the inversion and to disseminate the information from regions with high data content to adjacent, less directly constrained regions. Although we acknowledge the lack of objective quantification of the flux correlations in the emission inventories, we presented here a source-specific correlation set, exploiting the particular features of each emission category. The grid-based framework is found to improve the quality of the inversion, and in particular the geographical patterns of the emission updates, compared to the big region analysis.

[79] Although the grid-based inversion appears to be very promising for constraining the emissions of CO or other compounds, a large number of independent observations are needed to fully constrain all control parameters of the inversion. Even in this case, however, it remains difficult to distinguish between different emission categories (anthropogenic, biomass burning, biogenic), especially in tropical regions, where biomass burning and biogenic emissions are dominant, and their spatial and temporal distributions are most uncertain. A better identification and quantification of the sources will require either a better characterization of the prior emissions, or the use of additional constraints, e.g., chemical observations of additional compounds (e.g., formaldehyde) produced by basically the same sources as carbon monoxide.

[80] **Acknowledgment.** This work has been supported by the PRODEX programme of the ESA funded by the Belgian Science Policy Office, as well as by the EU FP5 project Evergreen (EVG2-2001-00051).

References

- Allen, D., K. Pickering, and M. Fox-Rabinovitz (2004), Evaluation of pollutant outflow and CO sources during TRACE-P using model-calculated, aircraft-based, and MOPITT-derived CO concentrations, *J. Geophys. Res.*, *109*, D15S03, doi:10.1029/2003JD004250.
- Andreae, M. O., and P. Merlet (2001), Emission of trace gases and aerosols from biomass burning, *Global Biogeochem. Cycles*, *15*, 955–966.
- Arellano, A. F., P. S. Kasibhatla, L. Giglio, G. R. Van der Werf, and J. T. Randerson (2004), Top-down estimates of global CO sources using MOPITT measurements, *Geophys. Res. Lett.*, *31*, L01104, doi:10.1029/2003GL018609.
- Axelsson, O. (1994), *Iterative Solution Methods*, 654 pp., Cambridge Univ. Press, New York.
- Bergamaschi, P., R. Hein, C. Brenninkmeijer, and P. J. Crutzen (2000), Inverse modeling of the global CO cycle: 2. Inversion of $^{13}\text{C}/^{12}\text{C}$ and $^{18}\text{O}/^{16}\text{O}$ isotope ratios, *J. Geophys. Res.*, *105*, 1929–1945.
- Costen, R. C., G. M. Tennille, and J. S. Levine (1988), Cloud pumping in a one-dimensional model, *J. Geophys. Res.*, *93*, 15,941–15,944.
- Crawford, J. H., et al. (2004), Relationship between Measurements of Pollution in the Troposphere (MOPITT) and in situ observations of CO based on a large-scale feature sampled during TRACE-P, *J. Geophys. Res.*, *109*, D15S04, doi:10.1029/2003JD004308.
- Deeter, M. N., et al. (2003), Operational carbon monoxide retrieval algorithm and selected results for the MOPITT instrument, *J. Geophys. Res.*, *108*(D14), 4399, doi:10.1029/2002JD003186.
- Dey, S., S. Tripathi, R. Singh, and B. Holben (2004), Influence of dust storms on the aerosol optical properties over the Indo-Gangetic basin, *J. Geophys. Res.*, *109*, D20211, doi:10.1029/2004JD004924.
- Emmons, L. K., D. A. Hauglustaine, J.-F. Müller, M. A. Carroll, G. P. Brasseur, D. Brunner, J. Stachelin, V. Thouret, and A. Marengo (2000), Data composites of tropospheric ozone and its precursors from aircraft measurements, *J. Geophys. Res.*, *105*, 20,497–20,538.
- Emmons, L. K., et al. (2004), Validation of Measurements of Pollution in the Troposphere (MOPITT) CO retrievals with aircraft in situ profiles, *J. Geophys. Res.*, *109*, D03309, doi:10.1029/2003JD004101.
- Erickson, D. J. (1989), Ocean to atmosphere carbon monoxide flux: Global inventory and climate implications, *Global Biogeochem. Cycles*, *3*, 305–314.
- Friedl, R. R. (1997), Atmospheric effects of subsonic aircraft: Interim assessment report of the advanced subsonic technology program, *NASA Ref. Publ.*, *1400*.
- Giering, R. (2000), Tangent linear and adjoint biogeochemical models, in *Inverse methods in Global Biogeochemical Cycles*, *Geophysical Monogr. Ser.*, vol. 114, edited by P. Kasibhatla et al., pp. 33–48, AGU, Washington, D. C.
- Giering, R., and T. Kaminski (1998), Recipes for adjoint code construction, *Trans. Math. Software*, *24*, 437–474.
- Gilbert, J.-C., and C. Lemaréchal (1989), Some numerical experiments with variable storage quasi-Newton algorithms, *Math. Programm.*, *45*, 407–435.
- Granier, C., U. Neimeier, J.-F. Müller, J. Olivier, J. Peters, A. Richter, and J. Burrows (2003), Variation of the atmospheric composition over the 1990–2000 period, *POET Rep. 6*, EU Project EVK2-1999-00011, Serv. d'Aéron., Paris.
- Guenther, A., et al. (1995), A global model of natural volatile organic compound emissions, *J. Geophys. Res.*, *100*, 8873–8892.
- Guenther, A., B. Baugh, G. Brasseur, J. Greenberg, P. Harley, L. Klinger, D. Serca, and L. Vierling (1999), Isoprene emission estimates and uncertainties for the Central African EXPRESSO study domain, *J. Geophys. Res.*, *104*, 30,609–30,624.
- Hao, W. M., and M. H. Liu (1994), Spatial and temporal distribution of tropical biomass burning, *Global Biogeochem. Cycles*, *8*, 495–503.
- Heald, C. L., D. J. Jacob, D. B. A. Jones, P. I. Palmer, J. A. Logan, D. G. Streets, G. W. Sachse, J. C. Gille, R. N. Hoffman, and T. Nehrkorn (2004), Comparative inverse analysis of satellite (MOPITT) and aircraft (TRACE-P) observations to estimate Asian sources of carbon monoxide, *J. Geophys. Res.*, *109*, D23306, doi:10.1029/2004JD005185.
- Helmig, D. H., B. Balsley, K. Davis, L. R. Kuck, M. Jensen, J. Bogner, T. Smith, R. V. Arrieta, R. Rodriguez, and J. W. Birks (1998), Vertical profiling and determination of landscape fluxes of biogenic nonmethane hydrocarbons within the planetary boundary layer in the Peruvian Amazon, *J. Geophys. Res.*, *103*, 25,519–25,532.
- Holzinger, R., A. Lee, M. McKay, and A. H. Goldstein (2005), Seasonal variability of monoterpene emission factors for a ponderosa pine plantation in California, *Atmos. Chem. Phys. Discuss.*, *5*, 8791–8810.
- Houweling, S., T. Kaminski, F. Dentener, J. Lelieveld, and M. Heimann (1999), Inverse modelling of methane sources and sinks using the adjoint of a global transport model, *J. Geophys. Res.*, *104*, 26,137–26,160.
- Intergovernmental Panel on Climate Change (IPCC) (2001), *Climate Change, The Scientific Basis (Contribution of Working Group 1 to the*

- Third Assessment Report of the Intergovernmental Panel on Climate Change*, edited by J. T. Houghton et al., Cambridge Univ. Press, New York.
- Jacob, D. J., B. D. Field, Q. Li, D. R. Blake, J. de Gouw, C. Warneke, A. Hansel, A. Wisthaler, H. B. Singh, and A. Guenther (2005), Global budget of methanol: Constraints from atmospheric observations, *J. Geophys. Res.*, *110*, D08303, doi:10.1029/2004JD005172.
- Kaminski, T., P. J. Rayner, M. Heimann, and I. G. Enting (2001), On aggregation errors in atmospheric transport inversions, *J. Geophys. Res.*, *106*, 4703–4715.
- Kanakidou, M., et al. (1998), 3-D global simulations of tropospheric chemistry with focus on ozone distributions, Results of the GIM/IGAC inter-comparison 1997 exercise, *EUR 18842*, Eur. Comm., Energy, Environ. and Sustainable Dev., Brussels.
- Kasibhatla, P., A. Arellano, J. A. Logan, P. I. Palmer, and P. Novelli (2002), Top-down estimate of a large source of atmospheric carbon monoxide associated with fuel combustion in Asia, *Geophys. Res. Lett.*, *29*(19), 1900, doi:10.1029/2002GL015581.
- Kuhn, U., S. Rottenburger, T. Biesenthal, A. Wolf, G. Schebeske, P. Ciccioli, E. Brancaleoni, M. Frattoni, T. M. Tavares, and J. Kesselmeier (2004), Seasonal differences in isoprene and light-dependent monoterpene emission by Amazonian tree species, *Global Change Biol.*, *10*(5), 663–682.
- Law, K., P. H. Plantévin, V. Thouret, A. Marengo, W. A. H. Asman, M. Lawrence, P. Crutzen, J.-F. Müller, D. Hauglustaine, and M. Kanakidou (2000), Comparison between global chemistry transport model results and measurement of ozone and water vapour by Airbus In-service Aircraft (MOZAIC) Data, *J. Geophys. Res.*, *105*, 1503–1525.
- Lobert, J. M., and J. M. Harris (2002), Trace gases and air mass origin at Kaashidhoo, Indian Ocean, *J. Geophys. Res.*, *107*(D19), 8013, doi:10.1029/2001JD000731.
- McDonald, R. C., and R. Fall (1993), Detection of substantial emissions of methanol from plants to the atmosphere, *Atmos. Environ.*, *27*, 1709–1713.
- Meirink, J. F., H. J. Eskes, and A. P. H. Goede (2005), Sensitivity analysis of methane emissions derived from SCIAMACHY observations through inverse modelling, *Atmos. Chem. Phys. Discuss.*, *5*, 9405–9445.
- Müller, J.-F. (1992), Geographical distribution and seasonal variation of surface emissions and deposition velocities of atmospheric trace gases, *J. Geophys. Res.*, *97*, 3787–3804.
- Müller, J.-F., and G. Brasseur (1995), A three-dimensional chemical transport model of the global troposphere, *J. Geophys. Res.*, *100*, 16,445–16,490.
- Müller, J.-F., and T. Stavrou (2005), Inversion of CO and NO_x emissions using the adjoint of the IMAGES model, *Atmos. Chem. Phys.*, *5*, 1157–1186.
- Nocedal, J., and S. J. Wright (1999), *Numerical Optimization*, Springer, New York.
- Olivier, J. G. J. (2002), Part III: Greenhouse gas emissions. 1. Shares and trends in greenhouse gas emissions; 2. Sources and methods: Greenhouse gas emissions for 1990 and 1995, in *CO₂ Emissions From Fuel Combustion 1971–2000*, pp. 1–31, Int. Energy Agency, Paris.
- Olivier, J. G. J., and J. J. M. Berdowski (2001), Global emissions sources and sinks, in *The Climate System*, edited by J. Berdowski, R. Guicherit, and B. J. Heij, pp. 33–78, A. A. Balkema, Brookfield, Vt.
- Olivier, J. G. J., J. J. M. Berdowski, J. A. H. W. Peters, J. Bakker, A. J. H. Visschedijk, and J.-P. J. Bloos (2001), Applications of EDGAR: Including a description of EDGAR 3.0: Reference database with trend data for 1970–1995, *RIVM Rep. 773301 001/NOP Rep. 410200 051*, Rijksinst. voor Volksgezondheid en Milieu, Bilthoven, Netherlands.
- Olivier, J., J. Peters, C. Granier, G. Pétron, J.-F. Müller, and S. Wallens (2003), Present and future surface emissions of atmospheric compounds, POET Report#2, EU project EVK2-1999-00011.
- Olson, J. S. (1992), World Ecosystems (WE1.4): Digital Raster Data on a 10-minute Cartesian Orthogonal Geodetic 1080 × 2160 grid, in *Global Ecosystems Database, Version 2.0*, Natl. Geophys. Data Cent., Boulder, Colo.
- Palmer, P., D. J. Jacob, D. B. A. Jones, C. L. Heald, R. M. Yantosca, and J. A. Logan (2003), Inverting for emissions of carbon monoxide from Asia using aircraft observations over the western Pacific, *J. Geophys. Res.*, *108*(D21), 8828, doi:10.1029/2003JD003397.
- Peters, J. A. H. W., and J. G. J. Olivier (2003), EDGAR3/POET emissions: 1997; Emissions and scenarios for 1995–2020; technical background information on global and regional sectoral emissions, *Rep. 77330103/2003* (digital version only), Rijksinst. voor Volksgezondheid en Milieu, Bilthoven, Netherlands.
- Pétron, G., C. Granier, B. Khattatov, J.-F. Lamarque, V. Yudin, J.-F. Müller, and J. Gille (2002), Inverse modeling of carbon monoxide surface emissions using climate monitoring and diagnostics laboratory network observations, *J. Geophys. Res.*, *107*(D24), 4761, doi:10.1029/2001JD001305.
- Pétron, G., C. Granier, B. Khattatov, V. Yudin, J.-F. Lamarque, L. Emmons, J. Gille, and D. Edwards (2004), Monthly CO surface sources inventory based on the 2000–2001 MOPITT satellite data, *Geophys. Res. Lett.*, *31*, L21107, doi:10.1029/2004GL020560.
- Plaza, J., L. Núñez, M. Pujadas, R. Páez-Pastor, V. Bermejo, S. Garcia-Alonso, and S. Elvira (2005), Field monoterpene emission of Mediterranean oak (*Quercus ilex*) in the central Iberian Peninsula measured by enclosure and micrometeorological techniques: Observation of drought stress effect, *J. Geophys. Res.*, *110*, D03303, doi:10.1029/2004JD005168.
- Randerson, J. T., M. V. Thompson, T. J. Conway, I. Y. Fung, and C. B. Field (1997), The contribution of terrestrial sources and sinks to trends in the seasonal cycle of atmospheric carbon dioxide, *Global Biogeochem. Cycles*, *11*, 535–560.
- Rinne, J., A. Guenther, J. Greenberg, and P. Harley (2002), Isoprene and monoterpene fluxes measured above Amazonian rainforest and their dependence on light and temperature, *Atmos. Environ.*, *36*, 2421–2426.
- Rödenbeck, C., S. Houweling, M. Gwloor, and M. Heimann (2003), CO₂ flux history 1982–2001 inferred from atmospheric data using a global inversion of atmospheric transport, *Atmos. Chem. Phys.*, *3*, 1919–1964.
- Rodgers, C. D. (2000), *Inverse Methods for Atmospheric Sounding, Theory and Practice, Ser. Atmos. Oceanic Planet. Phys.*, vol. 2, World Sci., Hackensack, N. J.
- Rossov, W. B., A. W. Walker, D. E. Beuschel, and M. D. Roiter (1996), International Satellite Cloud Climatology Project (ISCCP) Documentation of New Cloud Datasets, *Rep. WMO/TD-737*, 115 pp., World Meteorol. Org., Geneva.
- Savage, N., et al. (2003), Intercomparison of chemistry-transport models, *POET Rep. 2*, EU Proj. EVK2-1999-00011, Serv. d'Aéron., Paris.
- Smolarkiewicz, P. K., and P. J. Rasch (1991), Monotone advection on the sphere: An Eulerian versus semi-Lagrangian approach, *J. Atmos. Sci.*, *48*, 793–810.
- Staudt, M. C. Mir, R. Joffre, S. Rambal, A. Bonin, D. Landais, and R. Lumaret (2004), Isoprenoid emissions of *Quercus* spp. (*Q. suber* and *Q. ilex*) in mixed stands contrasting in interspecific genetic introgression, *New Phytol.*, *163*, 573–584.
- Takemura, T., T. Nakajima, O. Dubovik, B. Holben, and S. Kinne (2002), Single-scattering albedo and radiative forcing of various aerosol species with a global three-dimensional model, *J. Clim.*, *15*, 333–352.
- Tarvainen, V., H. Hakola, H. Hellén, J. Bäck, P. Hari, and M. Kulmala (2005), Temperature and light dependence of the VOC emissions of Scots pine, *Atmos. Chem. Phys.*, *5*, 989–998.
- Torres, O., P. Bhartia, J. Herman, and Z. Ahmad (1998), Derivation of aerosol properties from satellite measurements of backscattered ultraviolet radiation, Theoretical basis, *J. Geophys. Res.*, *103*, 17,099–17,110.
- Trostdorf, C. R., L. V. Gatti, A. Yamazaki, M. J. Potosnak, A. Guenther, W. C. Martins, and J. W. Munger (2004), Seasonal cycles of isoprene concentrations in the Amazonian rainforest, *Atmos. Chem. Phys. Discuss.*, *4*, 1291–1310.
- Tsutsumi, Y., M. Yoshida, S. Iwano, O. Yamamoto, M. Kamada, and H. Morishita (2005), Atmospheric CO monthly mean concentration, Ryori/Yonagunijima, WMO WDCGG, JMA, Tokyo.
- Van der Werf, G. R., J. T. Randerson, G. J. Collatz, and L. Giglio (2003), Carbon emissions from fires in tropical and subtropical ecosystems, *Global Change Biol.*, *9*, 547–562.

J.-F. Müller and T. Stavrou, Belgian Institute for Space Aeronomy, Avenue Circulaire 3, B-1180, Brussels, Belgium. (jfm@aeronomie.be; trissevgeni.stavrou@bira-iasb.oma.be)